Physics – Uspekhi **61** (10) 980 – 999 (2018)

INSTRUMENTS AND METHODS OF INVESTIGATION

PACS numbers: **41.50.+h**, **42.79.–e**, 61.05.cj, **87.59.–e**

X-ray fluorescence imaging

V V Lider

DOI: https://doi.org/10.3367/UFNe.2017.07.038174

Contents

Abstract. Over the past two decades, numerous X-ray microbeam studies have been published addressing the nondestructive investigation of chemical element distribution in condensed heterogeneous media. Based on this literature, some aspects of the field are discussed in this paper, including X-ray focusing methods and various elemental imaging techniques: scanning and confocal X-ray fluorescence microscopy, full-field X-ray fluorescence microscopy, X-ray fluorescence tomography, and prospects for combining X-ray fluorescence imaging with other physical methods rested on using synchrotron radiation.

Keywords: X-rays, X-ray fluorescence, X-ray focusing optics, X-ray fluorescent microscopy, X-ray tomography, X-ray spectroscopy, synchrotron radiation

1. Introduction

In this article, by X-ray fluorescence imaging (XFI), we understand a totality of methods allowing the elucidation of spatial distribution of chemical elements contained in a sample of interest, viz. scanning X-ray fluorescence microscopy (SXFM), confocal X-ray fluorescence spectroscopy (CXFS), full-field X-ray fluorescence microscopy (FF-XFM), and X-ray fluorescence tomography (XFT). These methods proceed from the phenomenon of X-ray fluorescence excitation upon exposure of the sample to a high-energy X-ray beam. The characteristic X-ray spectrum emitted in the process is practically unambiguously associated with the sample atomic composition and makes it possible to determine (both qualitatively and quantitatively) its constituent elements with a good spatial resolution.

In electron microanalysis, proposed in 1949, fluorescent radiation is excited by sample irradiation with a focused electron beam. The main advantage of excitation by electrons is the small size of the probe (as a rule, below 1 μm) and the high efficiency of secondary radiation excitation, especially in the low-energy region. However, electron-induced excitation has some serious disadvantages. First, sample bombardment with electrons produces not only the characteristic spectrum of a given element but also intense bremsstrahlung radiation, which markedly reduces the concentration-related sensitivity of the method. Second, excitation by electrons is a surface-sensitive method and can be applied to study a thin layer of the sample.

Unlike electron-induced excitation, X-ray excitation of fluorescence provides possibilities for studying much larger samples, especially at high X-ray (XR) energies. Moreover, electron-induced excitation implies special preparation of the sample, which has to be conductive and placed in a vacuum. Electron microanalysis cannot be regarded as a nondestructive method, especially for biological objects. This accounts for the wide application of highly sensitive and nondestructive X-ray fluorescence imaging techniques for characterizing the objects with nonuniform distribution of chemical elements, reported in numerous recent publications. The large number of reviews concerning investigations in biomedicine [1–5], materials science [6], geology [7], paleontology and archeology [8, 9], environmental research [10–14], preserva-

---

V V Lider Shubnikov Institute of Crystallography, Federal Scientific Research Center ‘Crystallography and Photonics’,
Russian Academy of Sciences,
Leninskii prosp. 59, 119333 Moscow, Russian Federation
E-mail: lider@ns.crys.ras.ru

Received 17 May 2017, revised 3 July 2017
Uspekhi Fizicheskikh Nauk **188** (10) 1081 – 1102 (2018)
DOI: https://doi.org/10.3367/UFNr.2017.07.038174
Translated by Yu V Morozov; edited by A Radzig

tion of cultural heritage [9, 15–17], tomography [18–20], and X-ray optics [21, 22] confirms the popularity of X-ray fluorescence imaging.

Practically each of the above reviews highlights only a single aspect of this multifaceted technique, which does not give the reader a comprehensive idea of the specific features and possibilities of applying X-ray fluorescence imaging. The present review is designed to enlighten the reader about the matter in question.

2. Principles of X-ray fluorescence

Differences in the energies of electron binding to the atomic nucleus depend on the region or level they occupy. Individual electron shells are marked by the capital letters K, L, M, N, . . ., with the innermost shell being designated as the K-shell, the second inner one as the L-shell, etc. The K-shell is occupied by two electrons, while the L-shell has three sublevels and may host as many as eight electrons. The M-shell has five sublevels and may contain up to 18 electrons (Fig. 1a).

Absorption of X-ray radiation by matter is underlain by photon–electron interactions in the inner shells of an atom. As soon as the photon energy exceeds the binding energy of an electron to the nucleus (the excitation threshold), the electron can be expelled from the atom, producing a sharp rise (jump) in absorption of X-rays (Fig. 1b). The wavelength corresponding to the excitation threshold energy is called the absorption edge of a given element. The absorption edge is a characteristic feature of each chemical element, which allows uniquely identifying this element from its edge position on the absolute energy scale.

The knockout of an electron from the K-shell by electron bombardment or photon absorption ionizes the atom. Given that the resultant electron vacancy is filled with an electron from the L-shell, such a transition is accompanied by the formation of the K-series fluorescence spectrum. This process leaves a vacancy in the L-shell that, in turn, can be filled with an electron from the M-shell, which is accompanied by L-series emission (Fig. 1a).

The fact that the fluorescence quantum energy is dependent only on the electron energy levels specific to each element accounts for the so-called characteristic X-ray radiation. Because each atom possesses a finite number of levels between which transitions of only a given type are possible, characteristic X-ray radiation produces a discrete ruled spectrum ('a fingerprint') of a concrete element.

An important parameter is the dimensionless quantity S of X-ray absorption jump deduced as the ratio of linear attenuation coefficients right and left of the absorption edge. The absorption jump weakly depends on the ordinal number of an element ($S \sim 1/Z^{1/2}$). For example, for aluminum ($Z = 13$), $S_{\mathrm{K}} = 12.6$, and for lead ($Z = 82$), $S_{\mathrm{K}} = 5.4$. L-shell absorption jumps within the range of atomic numbers from 47 to 92 vary as follows: S_{LI} — from 1.23 to 1.11; S_{LII} — from 1.47 to 1.31, and S_{LIII} — from 3.55 to 2.22 [23].

The fraction of excited photon-emitting atoms is determined with the aid of the dimensionless parameter ω, called fluorescence yield, which increases with increasing the atomic number Z and the electron shell depth. By way of example, for the K-shell of elements with Z from 20 to 80, ω increases from 0.13 to 0.95, whereas for the L-shell of the same elements, from 0.01 to 0.38. The main factors restricting the application and sensitivity of the method are the predominance of electron scattering and the low fluorescence yield in the case of light elements, as well as difficulties encountered in working with soft X-ray radiation. The validity range of the method can be considered to extend to the minimum detection limit falling on carbon ($Z = 6$).

The intensity of the ith line of a fluorescence spectrum, I_i can be described by the following approximate formula [23]:

$$I_i \sim \omega_q \left(\frac{\lambda_0}{\lambda_i} \right) \left(1 - \frac{1}{S_q} \right) p_i c_A t \,, \tag{1}$$

where ω_q is the fluorescence yield, S_q is the absorption jump of the q-level, λ and λ_i are the wavelengths of primary radiation and the registered i-line of fluorescence spectrum, p_i is the i-line intensity fraction of the total intensity of all lines of the q-series emitted by element A with concentration c_A, and t is the fluorescence emission depth:

$$t \approx \left(\frac{\mu_0}{\sin \beta_0} + \frac{\mu_{\mathrm{fl}}}{\sin \beta_{\mathrm{fl}}} \right)^{-1} . \tag{2}$$

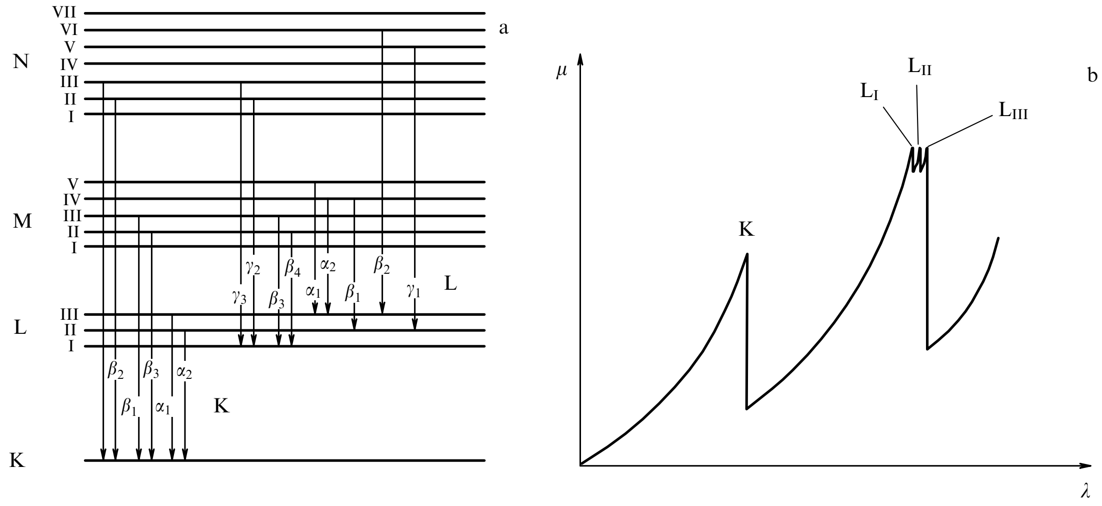

Figure 1. (a) Energy level diagram demonstrating all electronic transitions leading to the formation of K-, L-, and M-series. (b) Graph of X-ray absorption coefficient μ as a function of primary photon wavelength λ for the four absorption edges of X-ray radiation (K, $\mathrm{L_I}$, $\mathrm{L_{II}}$, and $\mathrm{L_{III}}$).

Here, μ_0, μ_{fl} are the linear absorption coefficients of primary and fluorescence radiation, while β_0 and β_{fl} are the respective angles between the input direction of primary radiation and output direction of fluorescence radiation and the sample surface.

Clearly, a vacancy in the q-shell cannot appear for $\lambda_0 > \lambda_q$ (λ_q is the wavelength of an absorption q-edge), and $I_i = 0$. I_i has the highest value at $\lambda_0 \approx \lambda_q$, of course if $\lambda_0 < \lambda_q$. I_i rapidly falls as λ_0 continues to decrease. This means that the highest intensity of fluorescence radiation from a given element can be achieved at a primary (exciting) radiation wavelength closest to the short-wavelength side of the absorption q-edge [23]. In a study of the elemental composition of bone tissue, the authors of Ref. [24] had to use a primary beam of synchrotron radiation (SR) with an energy of about 13.5 keV to detect heavy elements with high Z ($Z > 20$) and 3.15 keV to identify light elements with $Z < 20$. In Ref. [25], the high efficiency of light element excitation was reached using an X-ray tube with a chromium anode, in addition to a tube with a molybdenum anode.

Another useful parameter for estimating the efficiency of the method, the minimum detection limit C_{MDL} for each element, can be calculated from formula [26]:

$$C_{\text{MDL}} = \frac{3.29 C_Z (N_{\text{b}})^{1/2}}{N_{\text{s}}} . \tag{3}$$

Here, C_Z is the element concentration in the standard sample, N_{b} is the integral background intensity under the peak, and N_{s} is the integral intensity of the fluorescence peak. The lowest C_{MDL} values are obtained at a large $N_{\text{s}}/N_{\text{b}}$ ratio (good signal-to-background ratio and a high photon flux) and large N_{s}/C_Z ratio (effective fluorescence yield and high photon flux). For example, the use of SR to excite X-ray fluorescence can reveal up to 10^{-18} g of iron atoms in a sample [27, 28].

3. X-ray focusing optics

Spatial resolution is the key parameter for any X-ray imaging system. It usually depends on the sample thickness and fluorescence emission depth given by formula (2). This circumstance significantly restricts depth resolution [11, 13]. The spatial lateral resolution is largely determined by the size of the X-ray probe.

There are five main methods for the formation of a microfocal probe with the use of the following devices: an aperture diaphragm, Kirkpatrick–Baez mirrors, capillary optics, a Fresnel zone plate, and compound refractive lenses [5].

3.1 Aperture diaphragm

The simplest method to generate an SR beam with a small cross section ('pencil') is to avail oneself of an aperture diaphragm. The aperture is usually either a system of slits or a diaphragm of a given size, e.g., 0.1–1 mm. This method is most suitable for the collimation of a quasiparallel X-ray beam into a beam with a relatively large cross section. Such a transformation is frequently needed to facilitate the preliminary examination of a sample [29] or in investigating large-dimensional objects, such as objects of art [30, 31] and archaeological artifacts [32]).

3.2 Kirkpatrick–Baez mirrors

The very first acting X-ray optical systems were assembled from X-ray grazing mirrors with a large radius of curvature, taking advantage of total external reflection (TER) of X-rays [33]. The refractive index of XRs being smaller than unity, X-ray radiation incident on matter is totally reflected if the grazing angle θ is smaller than the critical angle θ_{cr}:

$$\theta_{\text{cr}} = \delta^{1/2} , \tag{4}$$

where $\delta = 1 - n = \rho \lambda^2 r_{\text{e}} N_{\text{A}} Z / 2\pi A$ (n is the XR refractive index), N_{A} is the Avogadro constant, r_{e} is the classical electron radius, A is the atomic weight of the element forming the sample material, and ρ is its density.

The first grazing incidence X-ray optical system capable of forming an image was proposed by Kirkpatrick and Baez [34] in 1948. It consists of two orthogonal elliptical mirrors, one of which focuses XRs into a line that is, in turn, focused onto a point by the other (Fig. 2a). Such a system was needed to avoid any astigmatism inherent in a single mirror. The elliptical shape of the working surface eliminates the spherical aberration characteristic of mirrors having a differently shaped working surface (cylindrical, toroidal). An advantage of the system is that the reflecting surfaces are easy to fabricate in the form of flat plates mechanically bent as appropriate [35]. Reference [36] reports the employment of mirrors with a rhodium-coated surface to enhance reflectivity

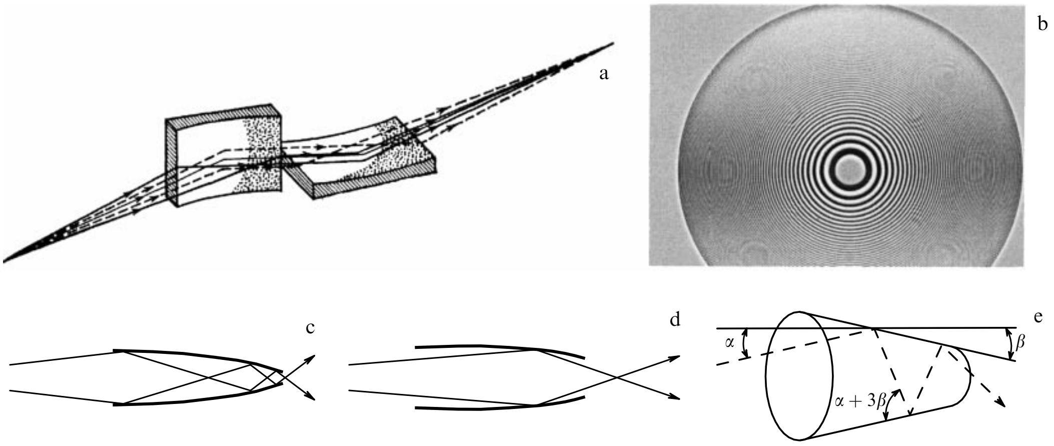

Figure 2. Optical elements used to focus XRs: (a) Kirkpatrick–Baez mirrors; (b) an image of a Fresnel zone plate obtained with the use of a scanning electron microscope (SEM) (diameter of 10 mm, $\delta r_N = 0.4$ μm) [21]; the paths of multiply (c) and singly (d) reflected rays in a monocapillary and (e) conical capillary [22] (see text).

($\sim 90\%$) of X-rays at a sliding angle of 3.5 mrad in an energy range (E) from 7 to 18 keV.

The mirrors can be artificial crystals composed of gradient multi-layers. In these mirrors, Bragg's law ($2d \sin \theta_B = \lambda$) must be satisfied at each point of the mirror surface. Because the Bragg angle (θ_B) varies along the entire length of the mirror, the interplane distance between the layers (d) must change laterally in accordance with a definite law [37, 38]. However, the bandpass of such a system is decreased ($\Delta\lambda/\lambda \sim 10^{-2}$).

Mirrors based on the TER phenomenon ensure submicrometer focusing of XRs [36, 39, 40]; sometimes the size of the focal spot can be reduced to tens of nanometers [41, 42]. The lateral resolution of a few dozen nanometers is also attainable for elliptical mirrors with a multilayer coating [43, 44].

3.3 Fresnel zone plates

Descriptions of the diffraction properties of the Fresnel zone plate (FZP) and references to relevant literature publications can be found in studies [45–48].

The FZP comprises a concentric set of alternate XR-absorbing and transmitting circumferential zones (Fig. 2b). Since diffraction has always to deal with several orders, it is necessary to consider them also in the case of FZP. The zero order ($m = 0$) represents unfocused radiation, whereas negative orders cover radiation divergently diffracted in different directions. High diffraction orders are characteristic of FZPs with different focal distances (to recall, even diffraction orders are forbidden for traditional FZPs). Usually, only the first-order diffraction ($m = 1$) is used as the brightest one, especially for the purpose of X-ray fluorescence microscopy.

Important FZP parameters include the width δr_N of the outer zone (N is the number of zones) that determines its Rayleigh resolution (diffraction resolution limit)

$$d_m = \frac{1.22\delta r_N}{m}\,, \tag{5}$$

and focal distance

$$f = \frac{4N(\delta r_N)^2}{m\lambda}\,. \tag{6}$$

The focal distance not only depends on the total number of zones N and the width of the outer zone, but also is inversely proportional to the wavelength; this suggests the presence of chromatic aberration, which means that in most applications FZPs must be exploited with monochromatic radiation. To eliminate chromatic aberration, the relative spectral width $\Delta\lambda/\lambda$ of radiation incident on the FZP must be smaller than the quantity equal to reciprocal of the number of zones multiplied by diffraction order m:

$$\frac{\Delta\lambda}{\lambda} \leqslant \frac{1}{mN}\,. \tag{7}$$

The dependence of the FZP focal distance on the XR energy may cause many problems in experiments with varying energy responsible for a change in the focal distance; there must be a possibility of moving the sample along the FZP optical axis to maintain it 'in focus'.

FZP efficiency η_m defines the proportion of XRs incident on an optical element and focused in diffraction order m:

$$\eta_m = \frac{1}{(\pi m)^2}\,. \tag{8}$$

For the first-order diffraction, the maximum efficiency equal to π^{-2} or $\sim 10\%$ corresponds to a traditional (classical) FZP. The remaining part of the radiation is either absorbed or utilized in other diffraction orders, viz. zero (25%), negative (12.5%), and high positive (2.5%) [45, 47].

One way to enhance the effectiveness of diffraction by an FZP is to replace nontransparent zones by transparent phase-shifting ones, so that radiation passing through them can also participate in focus formation [49]. Phase shift $\Delta\Phi$ accompanying the passage of XRs through a plate of thickness h depends on the decrement of XR refractive index δ:

$$\Delta\Phi = \frac{2\pi}{\lambda}\,\delta h\,. \tag{9}$$

The maximum efficiency is achieved when the phase shift equals π. This means that the electromagnetic field amplitude can be doubled with the resulting four-fold rise in the observable efficiency of focusing, from 10 to 40% for the first-order diffraction [50].

The finite initial size of the radiation source and optics of the experimental setup (electron storage device) account for the not absolutely coherent illumination of the FZP, which prevents obtaining a minimal focal spot [formula (5)]. In Ref. [51], 9.8-keV X-ray radiation was focused by an FZP with the diameter and the width of the outermost zone of 155 μm and 100 nm, respectively. The FZP was placed roughly 250 m from a storage ring undulator. This large distance made it possible to obtain a 200-nm focal spot (with a diffraction resolution limit of 122 nm). In Ref. [52], an FZP 160 μm in diameter with a 45-nm wide outer zone was used to focus XRs with an energy of photons of 10 keV onto a spot roughly 80 nm in diameter. Submicrometer resolution with the utilization of an FZP was reached in Refs [28, 53–57].

3.4 Capillary optics

Capillary X-ray optical systems make it possible to effectively generate X-ray beams of any desired configuration in a wide energy range. Furthermore, they are simple in design and manufacturing technology. The important feature of capillary optical elements is a high luminous intensity in comparison with other X-ray optics technologies, making it possible to use capillary systems not only for the transmission of information and images but also for designing an X-ray microscope with a high resolution power and radiation density.

Reference [58] showed that the inner surface of glass capillaries makes them suitable for application in X-ray optics. This means that such capillaries can be used as efficient waveguides for XRs, i.e., transporting wide-energy-range incoming radiation with losses that become appreciable only when there is a rather large number of reflections, because losses per reflection can be reduced to a minimum by choosing an adequate material and the quality of processing the inner surface of the capillary. For typical grazing angles $\theta \sim \theta_{\mathrm{cr}}/2$, the roughness height as a rule should not exceed 10–20 Å [59].

Figures 2c, d show the difference between two types of monocapillary optics: XRs are multiply reflected from the inner walls of the capillary and leave it after several sequential reflections. The size of a focal spot depends on the diameter of the outlet opening and source properties, while the efficiency is a function of the number of reflections, optics quality, and other characteristics; it usually varies from 10 to 80%. A disadvantage is the focus position very close to the exit from the capillary: to obtain a small (micrometer) focal spot, the sample must normally be placed within 10–100 outlet opening diameters, i.e., 10–100 μm.

A single-bounce capillary is needed to have a distance of several millimeters or centimeters between the focus and the outlet (Fig. 2d). The figure demonstrates an almost 100% XR transmission due to the high efficiency of single reflection under TER conditions [60].

To recall, the marked divergence of the beam at the exit from the capillary (up to the double TER critical angle θ_{cr}, e.g., 4.6 mrad at 13 keV) accounts for the size d_{f} of the focal spot greater than that of the outlet orifice d_{out} because of nonzero working distance f, i.e., the distance between the capillary end and the sample [58, 61]:

$$d_{\mathrm{f}} \approx d_{\mathrm{out}} + 2f\theta_{\mathrm{cr}}\,. \tag{10}$$

The optimal distance s between a point source and the capillary is given by the formula $s = (d_{\mathrm{in}}/2)\,\tan\theta_{\mathrm{cr}}$, where d_{in} is the inlet diameter of the capillary tube. If the space between the source and the capillary exceeds the optimal distance, the XRs that could participate in focus formation are lost, because the inlet angle of the capillary is smaller than the critical TER angle. For example, for a glass capillary with $d_{\mathrm{in}} = 10$ μm, one finds $s = 1$ mm [61].

Single-bounce monocapillaries usually have an elliptical or parabolic shape. The use of an elliptical capillary allows the point source to be focused if it is located at one of the ellipse focuses, with the focal spot appearing at the second focus. A parabolic capillary can either focus a parallel beam or transform an XR beam diverging from a point source into a parallel beam. In this case, the size of the focal spot depends not only on the quality of manufacturing the optical element, but also on the properties of the radiation source [62]. In Ref. [63], a 30-keV XR beam was focused using a single-bounce elliptical capillary onto a 15-μm focal spot.

One way to obtain submicrometer-scale X-ray beams is the use of conical capillaries narrowing in the elliptic or parabolic manner [21, 22, 64–67]. Reference [65] reports the achievement of a spatial resolution of 50 nm at $E = 5-8$ keV, the highest ever obtained using X-ray monocapillary optics.

XRs in a conical capillary (Fig. 2e) undergo TER from its smooth inner surface at the angles of incidence α smaller than the critical value θ_{cr}. The first reflection occurs at the angle $\alpha + \beta$, where β is the semivertex angle, the second and nth reflections at $\alpha + 3\beta$ and $\alpha + (2n-1)\beta$, respectively. If the angle of incidence exceeds the critical one, XRs do not participate in focus formation. Therefore, the number of effective reflections is given by the inequality $n < (\theta_{\mathrm{cr}} - \alpha + \beta)/2\beta$ [22, 61].

Capillaries can be applied not only to focus and transmit radiation, but also to change the direction of its propagation due to the possibility of keeping XRs within a slightly bent hollow capillary. Specifically bent capillary tubes allow XRs to be turned through an angle much larger than the critical one [59].

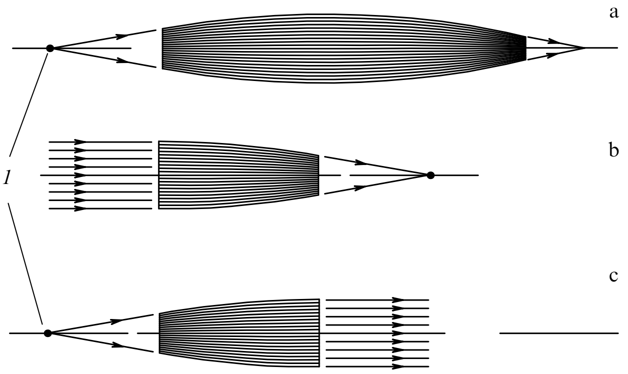

Figure 3. Kumakhov XR optics: (a) focusing lens: 'point source–focus'; (b) focusing half-lens: 'parallel beam–focus'; (c) half-lens: 'point source–quasiparallel beam' (*1* point source of XR) [71].

Tube bending requires taking into consideration that not all XRs entering the transmitting channel satisfy the condition $\theta < \theta_{\mathrm{cr}}$. Assuming the smallness of a capillary inner radius r_0 compared with the bending radius r_{curv} ($r_0/r_{\mathrm{curv}} \ll 1$) and taking account of the smallness of the TER critical angle for X-ray quanta, the condition for effective radiation capture in the capillary transport regime can be written out as

$$\frac{r_{\mathrm{curv}}}{r_0}\left(\frac{\theta_{\mathrm{cr}}}{2}\right)^2 \geqslant 1\,. \tag{11}$$

Thus, the maximum rotation angle $\Psi_{\max}$ of an X-ray beam in a capillary of length L is given by the expression

$$\Psi_{\max} = \frac{L}{r_0}\left(\frac{\theta_{\mathrm{cr}}}{2}\right)^2. \tag{12}$$

An X-ray lens can be assembled from a set of capillaries bent with different radii of curvature and arranged so that they direct radiation to a single point. Such a system is exemplified by a polycapillary lens (Kumakhov optics) having many bent surfaces [59, 68–73]. For each channel and mirror, the angle of radiation capture is smaller than a double critical angle; however, the real angle of capture can be as large as a few degrees (i.e., tens to hundreds of times greater than the critical angle).

Polycapillary Kumakhov optics permit either focusing a parallel flow (e.g., synchrotron radiation) or, conversely, obtaining quasiparallel radiation with XR divergence within a double critical angle from a finite source (X-ray tube) (Fig. 3).

One of the main parameters of polycapillary optics is the size of the focal spot being highly dependent on the working distance f [formula (10)]. The working distance must be large enough to provide the possibility of manipulating the sample. For example, the focal spot obtained with a polycapillary lens is 0.3–0.6 mm in size at an XR energy of 8 keV (CuKα spectral line) and $f = 5-10$ cm; for $f = 1-2$ cm and $f = 1-3$ mm, it can be reduced to 0.1 mm and less than 10 μm, respectively [70].

Another important parameter characterizing the efficiency of the optical system is the amplification factor G, defined as the ratio of radiation density in the focal spot formed by the lens to that generated by the source without the lens at the same distance from the source as the focal spot. The efficiency of a half-lens for obtaining a quasiparallel beam from a point radiation source can be estimated using equation [70]

$$G = \eta\left(\frac{\varphi}{\theta_{\mathrm{div}}}\right)^2, \tag{13}$$

where φ is the half-lens collecting aperture, θ_{div} is the beam divergence after passing through the half-lens, and η is the half-lens transmissivity (efficiency). For example, for the CuKα line ($E = 8$ keV), $\varphi \approx 0.1$ rad, $\theta_{\text{div}} = 5 \times 10^{-3}$ rad, $\eta \approx 0.2-0.3$ rad, and amplification factor G amounts to two orders of magnitude [70]. The authors of Refs [74] and [75] reported $G = 2500$ and 2970, respectively, for a glass polycapillary, i.e. significantly higher values than for a conical monocapillary ($G = 960$ at $E = 6$ keV) obtained in Ref. [66].

3.5 Compound refractive lenses

The multielement refractive lens is a relatively new optical system [76].

The real part of the refractive index in the X-ray range being smaller than unity, XRs can be focused by a double concave lens (Fig. 4a). As in traditional optics, the focal distance of such a lens is directly proportional to the radius of curvature R and inversely proportional to refractive index decrement δ. Due to the smallness of δ, the focal distance of a solitary lens for XRs is large enough (5–10 m at $E = 5-8$ keV), even when its radius of curvature R equals hundreds of micrometers. The large focal distance accounted for the absence of practical interest in refractive lenses. To enhance the refraction effect, the authors of Ref. [77] proposed a system consisting of a large number ($N > 100$) of coaxially aligned double concave lenses (Fig. 4b) that sequentially more strongly deflect XRs from their initial direction and thereby decrease the focal distance f:

$$f = \frac{R}{2N\delta}\,. \tag{14}$$

Such a multicomponent refractive lens from aluminum was used to focus a parallel X-ray beam with an energy of 14 keV ($\delta = 2.8 \times 10^{-6}$) onto an 8-μm spot within 1.8 m from the lens, enough for practical applications (the focal distance of a single lens would be 54 m). Simultaneously, photon flow density increased significantly as in the case of focusing by an optical lens [77].

If N is small, the lens can be regarded as transparent to XRs. Then, the amplification factor is calculated using the formula $G = 16\delta(f/\lambda)^{1/2}N$ [78].

Ideally, amplification can be 5,000-fold or even higher. In real lenses, it is much lower, and the focal spot is blurred due to lens defects and Compton and small-angle scattering [79]. The authors of Ref. [80] reported the value of $G \approx 100$ for an aluminum lens.

Today, many methods for manufacturing compound refractive lenses with a cylindrical refractive profile are available [78, 79], and various low-absorption materials have been tested. Aluminum lenses were examined in the XR energy range from 10 to 60 keV. XR absorption by aluminum makes these lenses inefficient at XR energies below 10 keV, and the number of lenses needed to focus XRs with energies above 60 keV grows progressively. Beryllium lenses can be used to focus XRs with an energy up to 2 keV.

Harder materials, e.g., nickel, are used in lenses at higher energies [81]. Nickel lenses can find application in work with SR at an energy up to 100 keV. Plastic systems have also been tested [82]. Compound lenses having a spherical profile composed of hollow balls (gas bubbles in a liquid) have also been proposed [83]. Further improvement in compound refractive lenses was based on applying the parabolic profiles to reduce spherical aberration [84]. The most advanced technologies make use of refractive profiles in the form of rotational paraboloids [81, 85].

To manufacture compound reflective lenses to focus a beam in two mutually perpendicular planes, rows of mutually perpendicular cylindrical holes are made in building blocks (Fig. 4c).

A beryllium lens of this type with the following parameters $R = 0.5$ mm, $N = 36.5 \times 37$, and $f = 1.82$ m at $E = 9.2$ keV formed a focal spot measuring 7.6×19 μm at $G = 13.6$ [79].

To sum up, the advantages of compound refractive lenses are as follows [79]: they are very strong, are simple to adjust and handle, have a small size ($\sim 5-10$ cm in length), have a focal distance and size that are easy to change by adding or removing monolenses, and are resistant to thermal impact. These features make them readily adaptable to work with undulatory radiation [86] using third-generation SR sources [87].

Even the lightest materials absorb XRs. The absorptive capacity determines the number of lenses that can be effectively combined within a compound optical element to avoid substantial losses and estimate the possible minimal size of the focal spot. In contrast, refractive planar kinoform lenses [76, 88–90] consisting of a set of parabolic segments focus XRs over a shorter 'free path' of radiation in a lens due to the removal of 'neutral' phase material responsible for the excessive 2π phase shift that significantly decreases XR absorption and thereby allows a theoretical 100% efficiency to be achieved. The segments have a common parabolic generatrix (Fig. 4d). The phase shift introduced by a segment equals $2\pi\delta x/\lambda$, where x is the segment thickness. This phase condition gives $x = \lambda/\delta$. The possibility of high resolution coupled to high efficiency makes kinoform lenses very attractive optical elements.

4. Fluorescence detectors

Because XRs posses both wave and corpuscular properties, they can be characterized in terms of wavelengths or energies. An energy-dispersive spectrometer that 'sorts' photons by

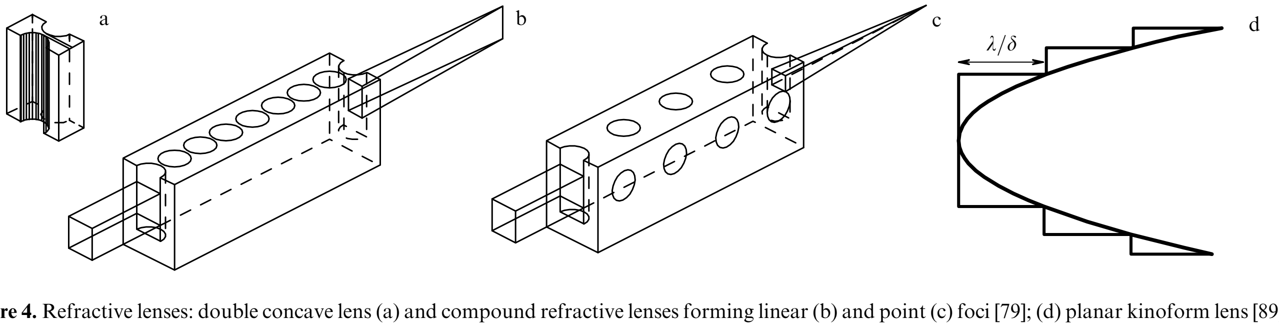

Figure 4. Refractive lenses: double concave lens (a) and compound refractive lenses forming linear (b) and point (c) foci [79]; (d) planar kinoform lens [89] (see text).

energies or a wavelength-dispersive spectrometer that grades X-ray radiation into wavelengths can be applied for the purpose of X-ray spectral analysis. In devices of the former type, radiation enters and is recorded directly in the detector. All the radiation is registered simultaneously: the electronic system distributes photons between the proper energy memory cells (channels).

The dispersive properties of the crystal lattice allow crystals to be used as analyzers of fluorescence obeying Bragg's law, which ensures enhanced energy resolution (the energy resolution of a (200)Ge crystal analyzer increases from 14 to 30 eV, as XR energy changes from 4 to 6 keV [91]). However, this method is inapplicable to the measurement of more than one X-ray energy at a time, which compromises the efficiency of data collection [92].

A variety of commercial solid-state energy-dispersive detectors are currently available, each with its merits and drawbacks [93, 94]. They all show good efficiency in a wide energy range, high energy resolution, and high counting rate. Germanium detectors ensure excellent energy resolution and high efficiency when used with high-energy XRs, even though the appearance of escape (parasitic) peaks may cause problems if the primary beam energy is above the germanium absorption K-edge ($E_K(\mathrm{Ge}) = 11.1$ keV).

Si(Li) detectors free from escape peaks provide an alternative to germanium ones. They also require cooling with liquid nitrogen. Their efficiency in the high-energy XR range is lower than that of Ge detectors, but higher that the efficiency of silicon drift detectors [5].

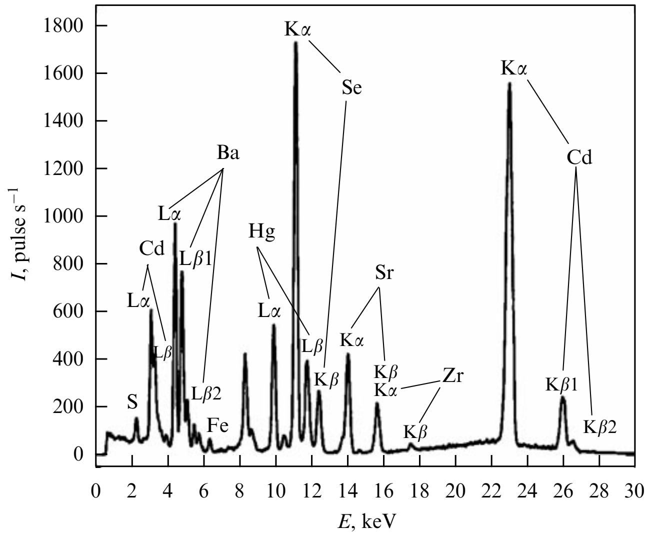

Figure 5. Fluorescence spectrum of an orange pigment contained in the paint layer of a canvas obtained with the aid of an SDD [94].

Silicon drift detectors (SDDs) have many attractive features, such as a high counting rate coupled to excellent energy resolution (as a rule, around 130 eV at $E = 5.6$ keV); moreover, they do not need liquid-nitrogen cooling. Figure 5 demonstrates the spectrum of an orange pigment contained in the paint layer of a canvas, obtained with the aid of an SDD. The virtually total absence of background permits individual chemical elements to be detected during the analysis of the composition of multicomponent materials.

The thickness of the devices being 450 μm, their efficiency in the high-energy XR region is low, which can be regarded as the main drawback of such detectors. Thicker devices more efficient in the high-energy X-ray region have recently been proposed [95].

The small size of the inlet window of SDDs is responsible for its restricted input solid angle. To solve the 'dead time' problem and increase the input solid angle, a system of several detectors can be used [96, 97], including monolithic backscatter detectors (Fig. 6a) with a large inlet solid angle and a small 'dead zone' for transmitting a primary X-ray beam [98–100]. The most popular of them is the MAIA detector [100], in which an annular array of 384 silicon detectors — each having an area of 1 mm^2 — provide a very large receiving solid angle.

5. Scanning X-ray fluorescence microscopy

Information on the two-dimensional (2D) distribution of chemical elements can be obtained by raster scanning analysis of a sample with respect to primary XRs focused onto a microspot. At present, this method, frequently referred to as scanning X-ray fluorescence microscopy (SXFM), is especially popular among researchers. It is implemented under experimental conditions in a 45°/45° geometry (Fig. 7) with the sample inclined 45° to the primary beam and the detector located in the storage ring plane (in the case of SR) at a right angle to the beam. Since SR is polarized in the horizontal plane, such a geometry reduces to a minimum the contribution from scattered primary radiation [102].

During measurements, a two-dimensional image of the sample is formed as it is transposed in the x and y directions (x and y are the orthogonal coordinates on the sample surface) with respect to the beam. The correlated movements of the sample and registering of the spectra permit gathering $n_x \times n_y$ individual fluorescence spectra (n_x, n_y are the number of pixels on the sample surface) that can be processed during or after collection of the data to make up elemental maps.

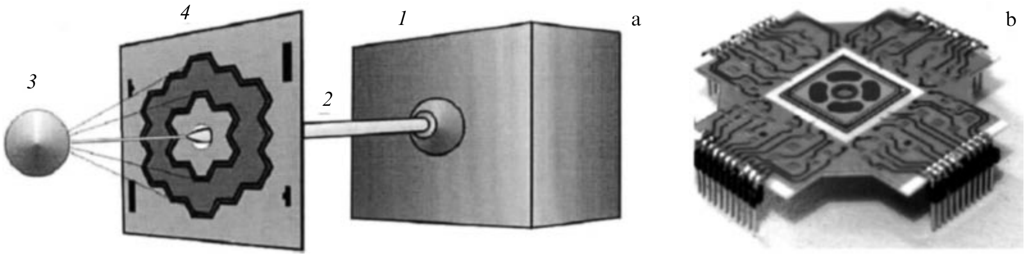

Figure 6. (a) Schematic of fluorescence analysis based on backscatter geometry: *1* is the XR source, *2* is the capillary focusing optics, *3* is the sample, *4* is the monolithic detector consisting of 12 SDDs with a total active area of 60 mm^2 [98]. (b) Photograph of a monolithic detector comprising four SDDs, each with an area of 15 mm^2 [99].

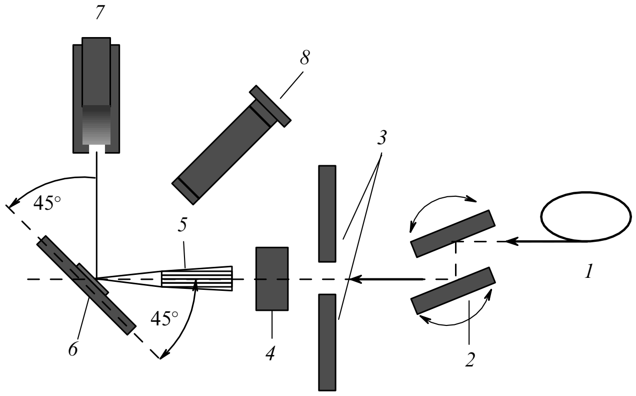

Figure 7. Typical setup for measurements by scanning fluorescence microscopy [101]: *1* is the SR source, *2* is the double-crystal monochromator, *3* is the slit system, *4* is the ionization chamber, *5* is the focusing optics, *6* is the sample, *7* is the solid-state energy-dispersive detector, and *8* is the light microscope.

The spatial resolution of XRF spectroscopy depends on the size of the focused X-ray beam, accumulated pixel intensity, scanning pitch, and the mode of scanning (stepwise or continuous) [5, 103]. The scanning pitch is of importance for resolution. The 50% overlap (the pitch size is half the focal spot size) is usually regarded as an opportunity to improve spatial resolution. In the case of a sufficient pixel intensity, the spatial resolution may become less than the spot size, but both these factors (pixel signal accumulation time and scanning pitch) considerably increase the duration of measurement.

The continuous scanning regime (on-the-fly scans) is rapidly replacing traditional methods of data collection in which the processing time and the mechanical movements of samples significantly increase the time needed for on the analysis. With on-the-fly scanning, the data are processed in real time without wasting additional time on the treatment of the data obtained [104]. Reducing of time spent to collect data and process them at each point (pixel) from a few seconds to fractions of a second implies the possibility of continuous movements of the sample instead of their interruption and resumption after completion of data collection.

SXFM taking advantage of SR has the following points in its merit over laboratory sources of XRs, such as X-ray tubes: high spatial resolution (up to a few dozen of nanometers), high elemental sensitivity (absolute detection limits reaching 10^{-18} g), the possibility of smoothly and/or rapidly changing the energy of exciting radiation, and the capacity to form a coherent (quasicoherent) X-rat beam.

On the other hand, this technique has limitations, like any other method. The major drawbacks are the bulkiness, high costs of the synchrotron and its operation, and the limited duration of an experiment. For instance, the time factor is responsible for the antagonism between the scanning area and the spatial resolution. The experimentalist has to choose between a comprehensive study of the region of interest (taking advantage of a small step size) and a low-resolution investigation of an extended area upon its exposure to X-rays beam (a useful description of criteria for the choice of the appropriate experimental station and designing an experiment was presented by Donner et al. [105]). The problem of time of analysis also arises from the risk of a radiation-induced defect in the sample [13, 104].

The above limitations and drawbacks of SR usage emphasize the importance of laboratory equipment for the experimental implementation of SXFM. The recent advent of high-brightness X-ray tubes, efficient X-ray optics, and fast-counting detectors provide the potential for the improvement of the analytical potential of laboratory instruments [106, 107], including commercial ones [103]. The application of laboratory instruments based on X-ray tubes for fluorescence imaging in the course of examining historical heritage and the analysis of depth distribution of various elements will be discussed below.

SXFM scans yield a data cube ($n_{\text{chan}} \times n_{\text{col}} \times n_{\text{row}}$), where n_{chan} is the number of channels in the energy-dispersive spectrum of each pixel of the image, and n_{row} and n_{col} are the numbers of rows and columns in the image [108]. Interpreting such 2D images is not a simple matter, because the intensity of characteristic X-ray radiation depends on the sample material and its 3D structure (usually unknown), which makes it difficult to determine the depth from which the data were obtained (near the surface or far from it). Moreover, the problem of processing large volumes of data arises [109]. Their treatment and utilization requires improved software support.

Full fluorescence spectra can be analyzed using AXIL [110] or PyMCA [111] packages. They make it possible to remove the background and resolve overlapping spectral lines. The PyMCA package guarantees preliminary visualization (e.g., determining the region of interest (ROI) from fluorescence raster maps) immediately after data loading.

SXFM is used to obtain both qualitative and quantitative information about elemental distribution in the sample. Quantitative X-ray spectral microanalysis based on a comparison of the measured intensity of X-ray lines generated in the sample of interest and the intensities of the respective lines in a standard sample of known composition under the identical analytical conditions (similar geometry of sample and standard positions, equal energy of primary beams, etc.) is called the external standard method. Quantitative elemental mapping and image processing are frequently performed using the MAPS package [112] or dynamic analysis [113] integrated into the Geo-PIXE software package [114].

This method is highly efficient and can be recommended for obtaining very accurate data. However, gauge standards can be used only for the analysis of samples of similar (if not identical) matrix compositions if matrix effects are disregarded. Indeed, the quantitation of the elemental composition in inhomogeneous samples may encounter additional problems:

(1) different matrix compositions in the sample and standard can be a cause of different degrees of absorption of primary and fluorescent XRs;

(2) most results obtained by the method are actually semiquantitative, because primary X-ray radiation penetrates rather deep under the surface of an inhomogeneous sample [115].

Starting from the studies of Sherman [116] and Shiraiwa, Fujino [117], the theoretical computation of X-ray fluorescence intensity has tended to develop as an analytical technique known under the name of the fundamental parameter method [118]. It makes use of equations describing XR-atom interactions to predict fluorescence spectra intensities emitted by samples having complex elemental compositions. Therefore, the quantitative analysis without

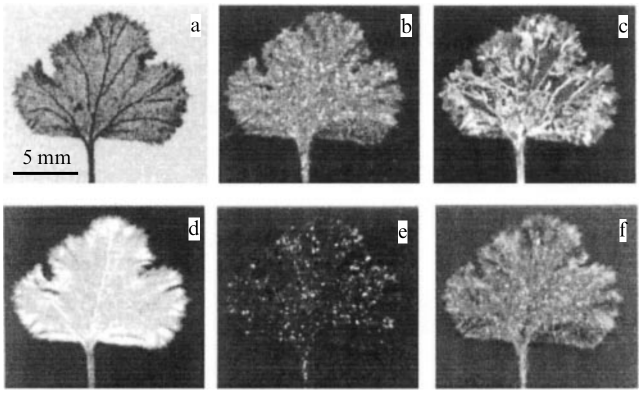

Figure 8. Image of a plant leaf taken from the garden near a metal refinery plant (a) and distribution of S (b), K (c), Ca (d), Ti (e), and Fe (f) [155].

standard samples can be the method of choice, even if its results are not very accurate [103].

The majority of current studies with applying SXFM are carried out in biology and medicine [119].

The cell is the smallest unit of life carrying genes and capable of autonomous existence, self-reproduction, and development. Therefore, cytology is the main field of research applying SXFM [36, 40, 42, 120–124].

Moreover, SXFM can be used to detect the metal microelements [125, 126] playing the key role in many biological systems [36, 42, 44, 121, 123, 127–133].

The method finds wide application in such areas of medicine as neurology and the treatment of neurodegenerative conditions [27, 101, 131, 134–137], oncology [41, 138–142], cardiology [143–145], ophthalmology [146, 147], osteology [39], and dentistry [148].

Metals can play an important role in natural processes proceeding in vegetable tissue (e.g., the participation of Mn in photosynthesis or the adverse effect of Cr on the growth of plants). The application of the method for studying the role of metal ions in plant physiology was considered in review [149] and Refs [13, 150–154]. Reference [155] presents XRF images of a plant leaf taken in the vicinity of an oil refinery plant (Fig. 8). The data available thus far indicate that the ability of plants to accumulate various chemical compounds can be employed for the evaluation of environmental pollution by means of SXFM.

Hair like plants can accumulate microelements and serve as useful bioindicators for the assessment of their influence on the human body, since they are easy to collect and store for a long time. SXFM was applied to analyze hair samples from mummified remains of two historical personages, Ferrante II of Aragon, King of Naples (1469–1496) and Isabella of Aragon, Duchess of Milan (1470–1524), allegedly poisoned with heavy metals. The results give reason to think that the metals were incorporated postmortem rather than as antemortem contaminants [156].

However, the level of microelements in hair does not always reflect their endogenous origin, because it can be influenced by pollution from exogenous sources, such as soil, dust, and water. The authors of Ref. [157] estimated the possibility of using hair as a bioindicator of microelement contamination based on elemental mapping of hair sections. They showed that the main elements, such as sulphur, are uniformly distributed across the section (Fig. 9c), whereas adsorbed metals concentrate on the surface without going deeper inside (Fig. 9a, b). These data suggest the necessity of a cautious interpretation of cases of poisoning with microelements, based on the analysis of human hair.

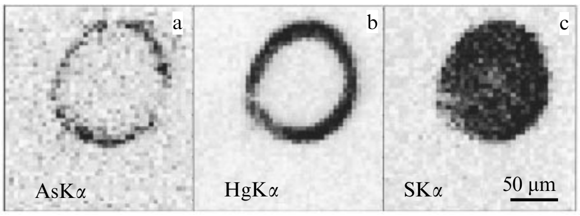

Figure 9. Distribution of microelements over a hair section subjected to chemical treatment [157].

Despite limitations, hair still remains an important material for pollution control, as it is easy to gather using a noninvasive procedure. To minimize limitations, hair samples should be washed prior to analysis to avoid over- or underestimation of pollution with poisonous microelements [157].

Let us turn now to the possibility of applying the method in other research fields.

Investigations into materials engineering [6, 158] were focused on fuel [159] and solar [52, 160–163] cells.

Geological studies were aimed at elucidating the nature of products of volcanic eruptions [164, 165] and the capture of various chemical elements by stalagmites during their formation. It was shown in paper [166] that annual Alpine stalagmite strata (Fig. 10) form due to variability of hydrologic conditions and variations in the duration of degradation of soil microbial communities. These findings can be used in paleoclimatology. On the other hand, there may be no direct correlation between a rise in the phosphorus level and its seasonal deposition, as was shown in some earlier studies, especially when the source of this element is other than an unstable phosphate formed as a result of leaching demineralization during seasonal vegetation diebacks in a moderate climate [167].

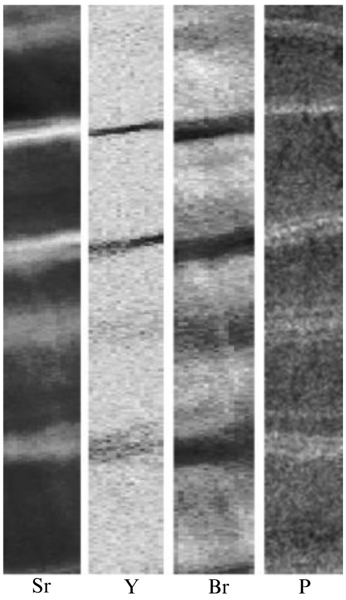

Figure 10. Maps of Sr, Y, Br, and P distribution in Alpine stalagmite (scan area: width 90 μm, height 700 μm). Dark regions correspond to high concentrations of elements [167].

Space exploration is exemplified by investigations of NWA 6693 meteorite fragments [165], cosmic dust samples, and particles captured from comet 81P/Wild 2 [168]. Of special interest in the field of environmental conservation are the studies of green concrete geopolymers [169] and mercury pollution in waterbodies [54]. Archeology took advantage of the SXFM method in studying fossilized fish [171, 172] and dinosaur [170] carcasses.

A large number of publications are devoted to investigations in the field of artistic and cultural legacy preservation. However, the large size of the objects of interest (e.g., paintings) makes it difficult to apply SXFM (described above and frequently called micro-SXFM) because of the small scanning area. It necessitated a transition to macro-SXFM [16]. The conflict between the scanning area size and the spatial resolution of macro-SXFM requires focusing XRs onto a spot 20 μm or more in size by a large-aperture polycapillary optics or the use of a 'pencil' beam 0.1–0.5 mm in diameter [15]. A series of useful studies was conducted at different synchrotron centers [8, 16, 30, 97, 173–176].

The sphere of SR-based macro-SXFM applications is limited by the lack of access to SR sources. Another obstacle is the necessity to transport paintings to SR centers and the related risks (theft, damage, suboptimal ambient conditions, etc.), as well as the associated high expenses (special means of transport and insurance). Finally, the size of the canvas is another limiting factor. An alternative approach to the application of macro-SXFM is the exploitation of mobile units built around X-ray tubes that can be delivered to a museum or a gallery for *in situ* studies.

The demand for such equipment stimulated the development of commercial units [15, 177]. Bruker Nano GmbH (Berlin, Germany) sequentially proposed and fabricated three variants of experimental units, ARTAX [178], Tornado M4 [103], and M6 Jetstream [177], based on microfocal X-ray tubes and polycapillary focusing optics providing a spatial resolution of at least 100 μm. The ARTAX system was designed largely for the point analysis of objects of cultural legacy. Moreover, it can be used for macro-SXFM applications [178], but the scanning area does not exceed 5×5 cm^2. Therefore, ARTAX is not fit to study large objects. Tornado M4 can be exploited to examine samples to a maximum of 20×16 cm in size. The use of the M6 Jetstream system allows the scanning area on a stationary object to be enlarged up to 80×60 cm using an X-ray beam, opening up prospects for investigating massive objects. This appears to be the main reason for the high demand for this technology [179–183].

X-ray optics is successfully employed to obtain small focal spots, but it is difficult to keep the sample surface in focus unless it is flat (e.g., pieces of sculpture or handiwork). The Kevex (Kevex Corporation, CA, USA) [184] eliminates this limitation by using an X-ray 'pencil' beam 50–500 μm in diameter.

Before and after the advent of readily available commercial equipment, certain research teams created their own laboratory instruments to study objects of cultural heritage [31, 32, 97, 185–189], as exemplified by a series of publications reporting the discovery of an artwork hidden behind later layers of paint [31, 97, 173, 175, 180, 190–193]. However, hidden images are usually spoiled by artifacts of their treatment, peculiarities of the surface paint layer, and the presence of regions lacking original information. Anitha et al. [194] proposed methods for restoration of such images.

A thorough examination of the paint layer by the macro-SXFM technique can be used to confirm the authenticity of an artwork [173, 188, 195, 196], identify materials and techniques applied by the artist to create the picture, and gain an insight into the creative process [31, 174, 181, 182]. Thus, an investigation of Leonardo da Vinci's portrait of "*La Belle Ferronniere*" revealed the discrepancy between elemental maps of Fe and Cu distributions (Fig. 11a, c) and inexact overlap of their contours. It was concluded based on these findings that the two different layers, one containing iron and the other copper, were applied one by one, sequentially, to form the background. Moreover, a thorough examination of dark regions of the background allowed the

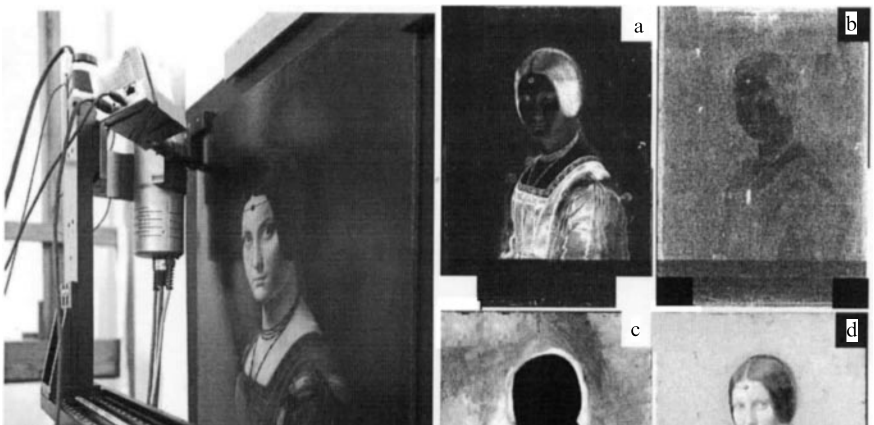

Figure 11. Macro-SXR microscope in front of Leonardo da Vinci's portrait of "*La Belle Ferronniere*" in the Louvre (left). Elemental maps in the rays of FeKα (a), CaKα (b), CuKα (c), and FeKα (inverse intensity on a logarithmic scale) (d) spectral lines [31].

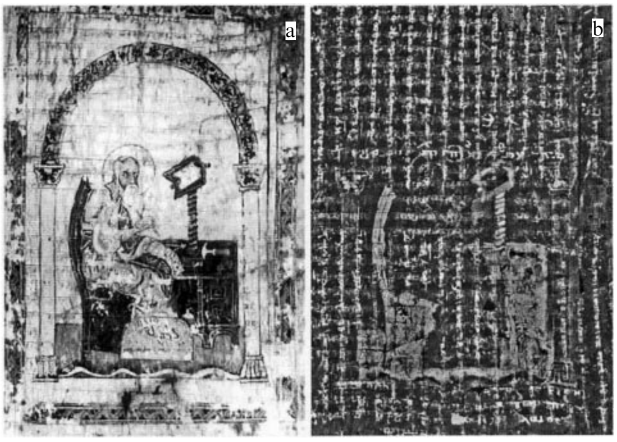

Figure 12. A palimpsest page painted over with a portrait in the 13th century readable in visible light (a) and FeKα rays (the X-ray technique picked up the iron in the ink) (b) [198].

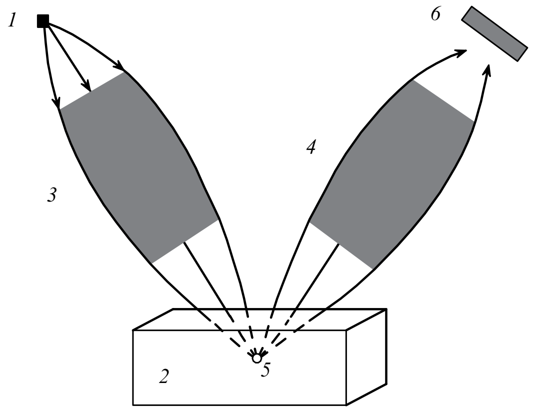

Figure 13. Schematic of a confocal X-ray fluorescence spectrometer: *1* is the source of X-ray radiation, *2* is the sample, *3* is the polycapillary lens focusing primary radiation, *4* is the polycapillary lens directing fluorescence radiation from confocal volume *5* to detector *6*.

presence of any other composition, drawing, or shading to be ruled out. Scanning of the lower part of the face also provided interesting information. Previous studies gave evidence that the artist had painted it in two steps. First, he applied a paint layer by modulating warm tones from pink to dark-red, largely with the aid of hematite identified from XR diffraction patterns. Then, the artist used varnish containing soot and white lead paint, which produced 'cold' white-to-black modulation. This layer was extremely thin (a few micrometers) to allow the underlying warm tone to show through to varying degrees. The microscopic study of this region revealed damage at least to the 'cold' varnish layer, probably caused by previous unskilful cleaning. The inverse intensity of iron on a logarithmic scale (Fig. 11d) demonstrates an extraordinary small hematite concentration gradient that forms the image of this part of the face. It can be concluded that the warm paint layer is unaffected; only a very thin layer of cold varnish is damaged. This result strengthened the decision to confine the intervention to delicate inpainting in the lower part of the face of "*La Belle Ferronniere*" [31].

Laboratory setups for macro-SXFM provide excellent tools for the analysis of documents, ancient manuscripts, and texts, including establishing their identity [8, 183, 197]. For example, an analysis of the parchment palimpsestnogo code showed a previously hidden vertical text (Fig. 12b), which was recorded in the 10th century in Byzantium, part of the treatise of Archimedes; in the 13th century, parchment was used again to write Christian liturgical texts (Fig. 12b). The erasure was incomplete, and Archimedes's work is now readable in images produced by X-ray fluorescence [198].

6. Confocal X-ray fluorescence spectroscopy

One of the challenging problems facing researchers is the analysis of objects with an inhomogeneous distribution of chemical elements not only over the surface but also in their innermost parts, e.g., objects having a layer structure. In the early 1990s, Gibson and Kumakhov [70, 199] proposed to address this problem using confocal X-ray fluorescence spectroscopy (CXFS) [20, 200–202] with spatial filtration to cut off out-of-focus radiation from part of the sample (background illumination). Besides optics focusing primary radiation, CXFS makes use of an additional optical element placed between the object and the detector for sampling fluorescence radiation absorbed in the bulk. This permits recording both fluorescence and scattered radiation coming only from the bulk region where optical foci of X-ray optics elements overlap (the so-called confocal volume) shaped like an ellipsoid. X-ray optics (a polycapillary lens (half-lens), a monocapillary, Kirkpatrick–Baez mirrors, and a compound refractive lens) focus primary radiation. The choice of optical devices for the detection channel is limited by a rather large angle of the fluorescence radiation collection and the broad energy range of radiation transmission, accounting for the use of a polycapillary lens (half-lens) or a conical collimator [203] to allow fluorescence radiation to be 'gathered' and directed toward the inlet opening of the detector (Fig. 13).

Although the use of SR in combination with confocal XRF demonstrated the high potential of the method, but the limited availability of the relevant equipment stimulated investigations in configurations with laboratory sources [25, 201, 204–208].

Tabletop XR sources emit many fewer photons than SR sources, which accounts for a roughly one or two orders of magnitude lower elemental sensitivity of the former [209]. However, the difference in the brightness of radiation sources hardly influences the resolving power of the method. By way of example, for an optical configuration formed by two polycapillary lenses (Fig. 13) of a laboratory setup [210], the size of the focal spot was experimentally found to equal 10 μm at an energy of 17.4 keV (MoKα), while the depth resolution varied between 22.6 and 13.7 μm as the XR energy changed from 5.4 to 11.4 keV, respectively (the critical TER angle decreased with increasing energy, so that radiation could be collected from a smaller volume). The involvement of SR allowed the authors of Ref. [211] to obtain a confocal volume measuring $15 \times 15 \times 20$ μm at an XR energy of 17.2 keV. To recall, the lateral and depth resolutions depend of the parameters of the focusing optics placed in front of the sample and the detector, respectively. The use of focusing optics, such as Kirkpatrick–Baez mirrors or compound refractive lenses, can appreciably improve lateral resolution [212].

Several methods have been developed for the quantitative analysis of CXFS [75, 205, 213–225]. The fundamental parameter method based on the assumption of isotropic confocal volume was designed for the analysis of paint layers [213]. The authors of Ref. [205] proposed an approach based on the correct modeling of the shape and size of the confocal volume. A new algorithm based on the fundamental parameter method and taking into consideration selected properties of a polycapillary was developed and applied for the study of microscopic particles of comet dust in Ref. [222]. A new iterative solution procedure based on the fundamental parameter method was proposed in Ref. [221] for the analysis of the composition and thickness of intermediate layers of stratified samples. A procedure for the quantitative reconstruction of a composition was designed and tested specially for such stratified materials [217]. It permits the chemical composition and thickness of individual layers to be determined. Sokaras and Karydas [218] simulated the secondary fluorescence effect in the analysis of multilayer structures. An alternative approach for simultaneous restoration of the composition and thickness of paint layers was proposed by de Viguerie et al. [219].

The main difficulty encountered in quantitative 2D-reconstruction is the necessity to simultaneously solve a huge number of nonlinear equations describing the relationship between mass fractions of various elements and the intensity of X-ray fluorescence radiation. A new iterative algorithm has recently been developed to avoid serious computational problems arising from simultaneous solution of equations in the fundamental parameter method [225].

CXFS has found application in various research fields.

Depth resolution is crucial when the sequence of layers composed of different elements is unknown, especially if this sequence changes along the sample surface. Therefore, the method found application in studying layer structures such as paintings [188, 213, 226–231] and handiwork [232, 233], as well as multilayer semiconductor devices [234]. The method is equally suitable for the study of metal corrosion [235, 236] and solid–liquid interfaces [237]. CXFS finds application in medicine [238, 239], geology [240, 241], archeology [242, 243], criminal science [244, 245], near and far space exploration [216], and pharmaceuticals, the mapping of different complexes in tablets being paramount for quality control and anticounterfeit technologies. References [246] demonstrated the possibility of tracing the distribution of certain inorganic elements (Zn, Fe, Ti, Mn, Cu) in a pill down to the depth of a few hundred micrometers and thereby excluding the influence of the coating material on the results of analysis and taking measurements of its thickness in the same experiment.

Sometimes, it is necessary to know the thickness and composition of the outer layer (envelope) of a study object. For example, Ref. [247] revealed an $\sim$ 80-μm thick outer layer in grains of rice enriched with metals. It was concluded that rice grown for food in areas polluted with heavy metals and other poisonous elements needs to be washed in a liberal amount of water prior to consumption.

7. Full-field X-ray fluorescence microscopy

In full-field X-ray fluorescence microscopy (FF-XFM), the primary X-ray beam is not focused but illuminates the entire surface of the sample. As a result, the sample emits fluorescent XRs that pass through a pinhole and fall freely onto the detector (Fig. 14). The pinhole creates, like a photographic camera-obscura, an inverted X-ray image of the sample [248–252]. The energy-dispersive charge-coupled device (pnCCD) plays the role of a detector chamber operating in the single-photon counting regime [253–258] and choosing an exposure so that the probability of finding more than one photon in the same pixel is insignificant. In this case, the signal is proportional to the energy of a fluorescent photon incident on the detector. In other words, pnCCD combines high spatial and energy resolution.

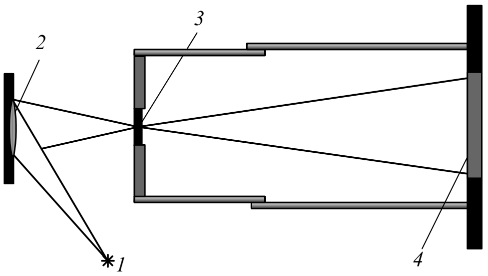

Figure 14. Optical setup of FF-XFM: *1* is the XR source, *2* is the sample region of interest, *3* is the pinhole, and *4* is the pnCCD detector [253].

The choice of pinhole diameter is a compromise between resolution and efficiency: a smaller hole improves resolution but reduces the number of photons incident on the detector. The minimal optimal diameter of the hole was found to be 30 μm [259] and 15 μm [248].

The authors of Refs [260–263] substituted the pinhole with a Wolter mirror, an axially symmetric tandem of conical mirrors with hyperboloid and ellipsoid working surfaces [264, 265]. The Wolter mirror ensures minimum comatic and zero chromatic aberrations. Moreover, its data acquisition efficiency is one or two orders of magnitude higher than that of the pinhole, while spatial resolution may reach 10 μm [260].

At present, FF-XFM is used rather seldom. Examples are studies of geological [259] and cultural heritage [266, 267] objects.

The new modification of this method proposed in Refs [268, 269] is based on the illumination of a sample cross section with a primary beam focused in a single plane, while fluorescence radiation collimated by the pinhole is recorded by the pnCCD detector (Fig. 15), allowing transverse

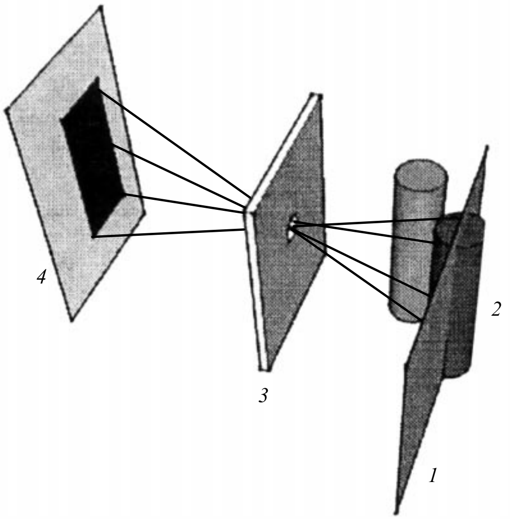

Figure 15. Optical setup of FF-XFM with the use of a flat beam: *1* is the flat beam, *2* is the study sample, *3* is the pinhole, and *4* is the pnCCD detector [268].

elemental images to be obtained from the depth of the sample limited by XR absorption effects alone. The method can be employed for thickness elemental visualization and X-ray fluorescence tomography.

8. X-ray fluorescence tomography

A set of methods known under the generic name tomography allows for nondestructive visualization of internal elemental distributions.

The term tomography derives from the Greek words 'to cut or section' (tomos) and 'to write' (graphein). So the main task of tomography is imaging by sections to reveal the internal structure of an object. It allows obtaining a series of two-dimensional images that are mathematically converted into 3D ones [270]. The most popular scanning X-ray fluorescence tomography (SXFT) usually yields 2D images by (x, y)-scanning of a sample rotated with a small pitch angle to obtain a series of two-dimensional elemental projections. The process is repeated at an angle interval of $0^\circ - 360^\circ$ or $0^\circ - 180^\circ$ and is completed when 2D sinograms of each element are produced (a sinogram is a two-dimensional image of all unidimensional projections of the object's layer as a function of the projection angle). The sinograms thus obtained are summed and combined for three-dimensional examination [18, 19, 57, 158, 271, 272]. Given that there is a large enough number of angular projections in all directions, it is possible to reconstruct images of the elemental distribution within a virtual 2D cross section (Fig. 16).

However, almost all stages of rotation give a 'yield' error when the axis of rotation shifts with a change in rotation angle. The error needs to be detected and corrected by aligning individual projections with the aid of various algorithms [273–278].

The filtered back-projection (FBP) algorithm was the first reconstruction algorithm used for SXFT [279]. However, iterative methods are frequently preferred for image reconstruction [280], because they usually decrease noise susceptibility and can reconstruct high-quality images when there are incomplete experimental data. Specifically, the algebraic reconstruction technique (ART) [281, 282] and expectation maximization (EM) algorithm [277, 283–285] have been extensively used. The accuracy of 3D reconstruction of elemental images is limited by XR absorption effect. Hogan and co-workers proposed an excellent compromise between the reconstruction rate and image quality [286]. Many tomographic techniques were based on simpler models that ignore multiple XR scattering but take account of the absorption of primary and fluorescence radiation [282, 287].

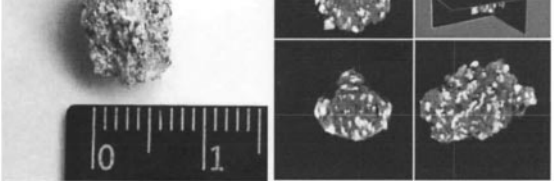

Figure 16. (a) Visual image of a sandstone sample, and (b) three virtual orthogonal images showing iron particle distribution (light regions) [249].

An iterative reconstruction method has recently been developed to restore fluorescent tomograms with reference to all attenuation effects (including those of repeated absorption of fluorescence radiation) without prior knowledge of radiation absorption by the sample [274, 288].

According to Ref. [249], iterative algorithms should be used to obtain reasonably good-quality 3D elemental images, e.g., the Poisson model-based maximum likelihood expectation maximization (ML-EM) algorithm [289].

Implementation of computed tomography using CXFS or FF-XFM techniques for a flat beam does not require sample rotation as in SXFT; it is performed by (x, y, z)-scanning or x-scanning (yz is the primary beam plane), respectively.

Such an approach simplifies reconstruction algorithms that are reduced to registrating the XR absorption effects and taking account of polycapillary optics properties. Another advantage of these two methods consists in the freedom of choosing the study area, allowing the analysis of a small site on a large sample. This makes preparation of the sample much easier than for SXFT and FF-XFM. Moreover, CXFS tomography makes it possible to obtain 3D elemental images of the sample in different angular positions (Fig. 17).

Nevertheless, most results have been obtained by SXFT. This method has been used in biomedicine to elucidate metal distribution in breast tissue samples [291, 292], to study perfusion in the mouse brain cortex, hypocampus, and thalamus [293], to investigate myocardial metabolism in hamsters [294], to measure bone mineral content [119], as well as the possibility of examining hydrated biological objects [295].

Subjects of environmental research have included fly-ash particles of municipal waste [296], mechanisms of the toxic action of transition metals (Cu, Ni, and Zn) on pelagic and benthic invertebrates [297], arsenic contamination of aquatic plants (*Ceratophyllum demersum*) [298], TRISO (TRistructural-ISOtropic)-coated fuel particles used in high-temperature gas-cooled reactors [299], Ni hyperaccumulation in plants (*Alyssum murale*) [300, 301], Fe, Zn, Mn, Ni, and Co distribution in longitudinal and transverse sections of apple

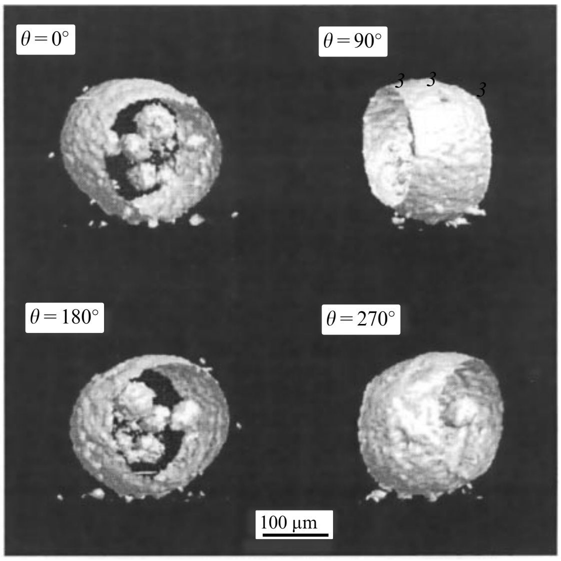

Figure 17. Iron distribution in an egg of the ecotoxicological model crustacean *Daphnia magna* for four different angular positions of the sample [290].

tree (*Malus xiaojinensis*) roots [302], and iron localization in the seeds of *Arabidopsis* [303].

9. Combined application of X-ray fluorescence imaging and other physical methods

Not infrequently, it is necessary to combine several experimental techniques, so that advantages of one make up for disadvantages of another. Each method, of value in itself, becomes a powerful tool if employed to study complex systems together with other techniques. One of the advantages of SR is the great variety of methods for its application. Whenever possible, different studies should be conducted using the same equipment. This rather natural approach allows integrating various X-ray methods. The present section is focused on co-utilization of different X-ray fluorescence imaging (XFI) modalities (mostly, SXFM and CXFS) with the use of one or more X-ray techniques based on the application of an SR microbeam [9, 304], viz. X-ray absorption fine structure spectroscopy (XAFS), X-ray diffraction (XRD), scanning transmission X-ray microscopy (STXM), coherent diffraction imaging (CDI), Fourier transform infrared scanning (FTIR), and X-ray beam-induced current (XBIC).

XFI/XAFS. Depending on the energy range, XAFS spectroscopy is divided into two components, low- and high-energy, called X-ray Absorption Near Edge Structure (XANES) and Extended X-ray Absorption Fine Structure (EXAFS), respectively [305].

As a rule, the XANES spectral region extends from ~ 10 eV below to ~ 40 eV above the absorption edge. Significantly more atoms are involved in the scattering process in the XANES regime than in the EXAFS, including atoms of both the first coordination sphere and spheres spaced far apart from the absorbing atom. The EXAFS provides information about the local environment of atoms in both solids and individual molecules; it also allows the surrounding atoms and the distance to them to be identified. Characteristics of the EXAFS method account for its extensive application in condensed matter physics and chemistry. XANES technique yields information on the degree of oxidation and the electronic structure of absorbers.

As is known, the position of the XR absorption edge highly depends on the degree of oxidation of the absorbing atom: it shifts to a higher energy region with increasing the degree of oxidation. Comparing the measured spectrum of the sample to that of a compound containing the absorbing atom with a known valence allows the charge state (valence) of a given atom in this compound to be determined. By combining XFI and XANES, one can obtain information not only about the concentration distribution of a given element but also about the degree of its oxidation.

In many cases, e.g., in studies on metal interactions with plants [13, 14, 152, 306–309] or experiments with medical objects [55, 148, 310–315], XAFS is implemented in 'transmission' geometry by choosing a point (points) for analysis on the elemental map obtained by SXFM. Because fluorescence radiation intensity is proportional to the absorption coefficient, which, in turn, depends on the element valence state, XAFS spectra can be recorded in the 'reflective' mode in the so-called fluorescence regime [161, 316–318]. Moreover, it is possible to determine the spatial distribution of each element in each oxidation state by adjusting, with the aid of a double-crystal monochromator (Fig. 18a), the excitation energy to absorption edge energies of standard samples containing the study element with the required valence [319–329], with subsequent collection of data and their adequate processing [319–321].

The fern *Pteris vittata* is known to accumulate very large amounts of arsenic. It was shown in Ref. [325] that arsenate (pentavalent As) is converted into even more toxic arsenite (trivalent As) in the leaves of the plant rather than in its roots, as had been thought before (Fig. 19). The energies for chemically defined images corresponded to edge absorption peaks of the standards: 11869.8, 11871.4, and 11874.8 eV for arsenic, arsenite, and arsenate, respectively.

XFI/STXM. Amplitude (absorption) X-ray contrast used in STXM is associated with variations in density and/or

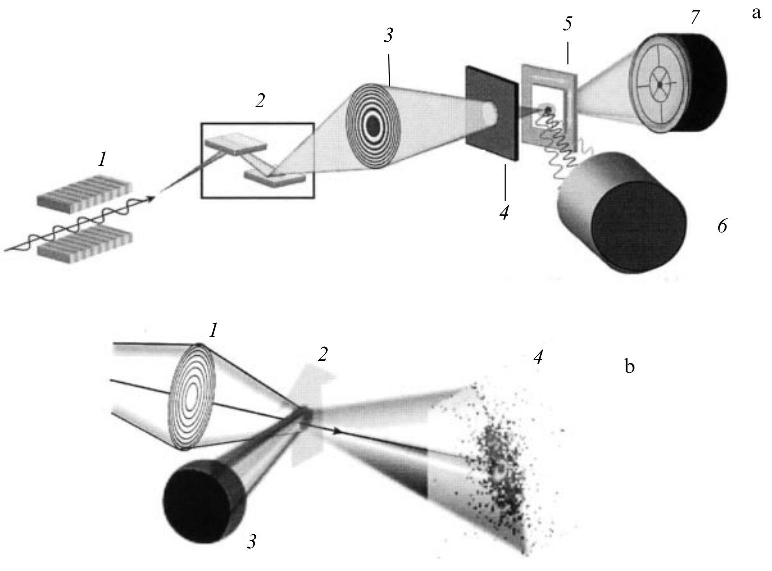

Figure 18. Schematic representation of experimental setups combining (a) XFI and STXM [331] (*1* is the undulator, *2* is the double-crystal monochromator, *3* is the FZP, *4* is the sorting diaphragm, *5* is the sample, *6* is the fluorescence detector, *7* is the segmented CCD detector); (b) XFI and CDI [334] (*1* is the FZP, *2* is the sample, *3* is the fluorescence detector, and *4* is the transmitted radiation detection plane).

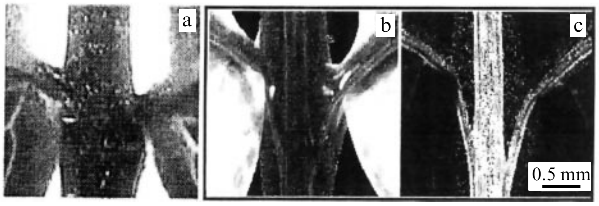

Figure 19. A fragment of stem and leaves of the fern *Pteris vittata* in visible light (a), arsenite (b) and arsenate (c) distributions (see the text).

thickness of neighboring regions of the sample of interest, which makes possible investigations of its morphological features and peculiarities of the internal structure.

The tomographic reconstruction of fluorescence can be used to determine the internal elemental composition of the sample. On the other hand, conventional X-ray projection microscopy can be employed to reconstruct the spatial distribution of the absorption coefficient in the sample. The authors of Ref. [278] combined X-ray fluorescence with X-ray transmission techniques and proposed an optimized approach to the reconstruction of the sample's elemental composition. The model allows the simultaneous reconstruction of the quantitative spatial distribution of all elements and the XR absorption effect in the sample. It was shown that the combined approach ensures better reconstruction of the elemental image than either method alone. Therefore, the problems arising from XR absorption effects in the sample are less pronounced in X-ray fluorescence tomography.

Figure 18a shows the layout of an experimental setup combining XFI and STXM. It makes possible simultaneous data collection, eases difficulties associated with using either method for this purpose, and provides more complete information about the sample, because functional images obtained with XFI are supplemented by morphological data provided by STXM [330]. The authors of Refs [57, 331, 332] used a segmented CCD detector to record XRs that passed through a sample [333]. One advantage of this device is the possibility of exploiting different combinations of its segments at a time, due to which single scanning of the sample gives enough data for the analysis of both the amplitude and the phase of the transmitted radiation: difference images between opposite segments define the differential phase contrast, while the sum of all signals yields the absorption contrast of the sample image.

The first two tomograms in Fig. 20 demonstrate absorption and differential phase contrasts of the diatom alga *Cyclotella meneghiniana*; the remaining eight illustrate the distributions of Si, P, S, K, Ca, Mn, Fe, and Zn [57].

The authors of Refs [331, 332] argue that differential phase contrast observed simultaneously with a fluorescence image can be used to improve the alignment of angular projections of the image with respect to the common rotation axis in low-intensity X-ray fluorescence tomography. This requires a larger number of projections with shorter exposure time to achieve a higher 3D resolution in the reconstructed tomogram than in the case of longer exposure with fewer projection angular positions.

XFI/CDI. A combination of coherent diffraction imaging (CDI) with XFI improves the phase contrast and spatial resolution, as well as quantitative elemental mapping. The experimental setup depicted in Fig. 18b is not substantially different from that usually used for XFI/STXM, the only distinction being the presence of a pixelized detector for recording transmitted radiation and the formation of a coherent (quasi-coherent) X-ray beam [334–336]. In Ref. [334], a 7.7-keV X-ray beam was focused onto a spot 250 nm in diameter using an FZP having a 100-nm wide peripheral region. The 50-μm aperture diaphragm placed 0.5 m in front of it guaranteed coherence of FZP lighting. The sample was scanned by a coherent beam with obvious overlapping.

XFI/XRD. A combination of microscopic X-ray fluorescence and X-ray diffraction microscopy provides a nondestructive tool allowing the visualization of the distributions of chemical elements and related crystalline phases in thick (millimeter-sized) multicomponent heterogeneous materials. XFI/XRD visualization combines an energy-dispersive detector for XFI placed 90° to the primary beam and a CCD detector with a large inlet 'in transmission' window used to record combinations of experimental data for XFI and XRD, respectively [63].

De Nolf and Janssens [63] studied a coating in the form of a multilayer car enamel by applying symbiotic XFI/XRD technique. The identified eight paint layers contained eight different crystalline substances. All the layers were distinguishable in XRD images, which allowed their average thickness to be calculated. Reference [337] demonstrated the heterogeneous distribution of radionuclides and metals in soil samples taken at mine sites in Central Asian regions of the former Soviet Union, while the authors of Ref. [338] investigated the nanostructure of alkali-activated metakaolin (potential cement substituent).

Figure 21 presents the results of investigations of Ti/B/C/Ni ceramics [339]. Partial spatial correlation is

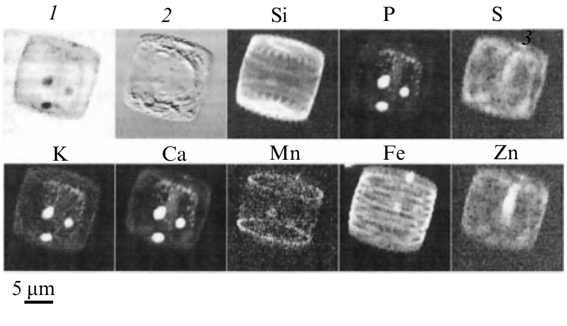

Figure 20. Elemental tomograms of the diatom alga *Cyclotella meneghiniana* (*1*, *2* are the tomograms of absorption and differential phase contrast, respectively) [57].

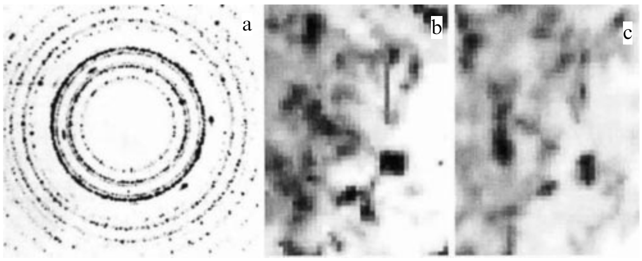

Figure 21. Diffraction pattern (a), Ni_3B phase map (total intensity of reflections [121], [122], and [221]) (b), and NiKα (XFI) spectral line intensity map (c) of Ti/B/C/Ni ceramics (scanning area size is 400×500 μm) [339].

documented between the Ni distribution near the sample surface and the Ni_3B phase map showing the projection of this phase distribution over the volume of the examined region. The two signals do not represent the same sample volume, which accounts for the considerable difference between both distributions.

XFI/XBIC. The XBIC technique not only reveals and characterizes electrically active extended defects in semiconductor crystals but, in combination with XFI, can provide information about the influence of the heterogeneous admixture distribution in the sample on its electrical properties. The combination of the two methods was used to study the activity of defect recombination and chemical origin in a silicon sample with high sensitivity and micrometer-scale spatial resolution [340]; moreover, it permitted revealing metallic impurities in a silicon photovoltaic cell [341].

XFI/FTIR. FTIR spectroscopy permits the identification of molecular groups in various media, including characteristic organic and inorganic materials, regardless of their crystalline or amorphous structure [16]. The authors of Ref. [342] took advantage of FTIR to show that the chemical composition of petrified reptilian skin differs from that of the sedimentary rock in which it was buried and retains its important composite features. Images obtained by XFI confirmed these results. The authors of Ref. [343] undertook the analysis of brain tissues from patients suffering from Alzheimer's disease.

XFI/XAFS/XRD. An experimental station allowing the simultaneous collection of data obtained by these three methods is shown in Fig. 22.

It turns out that the combination of XFI, XAFS, and XRD can be successfully used to study microelectronic systems [344], the environment [345–349], and objects of cultural heritage [16, 350].

XFI/XAFS/FTIR. This combination has been utilized in medicine [351] and cultural legacy objects [329].

XFI/XAFS/XBIC. These methods have been employed to estimate the size and spatial distributions, shape, electrical activity, and chemical composition of iron-rich precipitates in polycrystalline silicon materials, finding application in cost-efficient solar panels. Experimentally observed properties of iron-enriched precipitates provided insight into their origin and mechanism of coalescence in polycrystalline silicon, and permitted obtaining quantitative data on Fe and Si distributions and their influence on the work of solar cells. The available information suggests that the poor efficiency of some of these devices is not necessarily related to the total amount of the iron involved but depends on its distribution in the material [161]. Another publication (Ref. [352]) reports the results of investigations into the interaction between various admixtures in intentionally contaminated polycrystalline silicon samples. It was shown that Si_3N_4/SiC particles frequently found in polycrystalline silicon are efficient sinks for Fe and Cu impurities. The copper-containing compound was identified as silicide Cu_3Si.

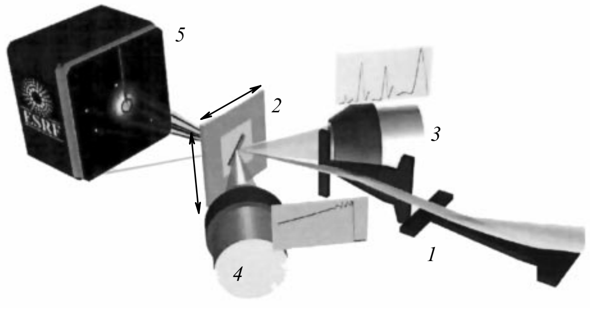

Figure 22. Experimental station combining XFI, XAFS, and XRD techniques: *1* is Kirkpatrick-Baez mirrors, *2* is the sample, *3*, *4* are the fluorescence and XAFS-spectra detectors, and *5* is the XRD detector [344].

XFI/XAFS/XRD/FTIR. These four methods make use of initial SR brightness, allowing having a focused X-ray beam with a size close to that determined by the diffraction limit (a few micrometers for infrared mid-regions of the spectrum and less than 1 μm for XRs). It suggests the possibility of obtaining a signal during a short-term exposure (from tens of seconds in FTIR to less than 1 s in XFI or XRD). The combination of these two aspects is of importance for obtaining two-dimensional high-resolution elemental maps.

Reference [353] deals with a long-standing problem concerning the role of cadmium carbonate and cadmium sulfide in the degradation of the paint layer in artwork. An assessment of the condition of the paint layers in Henri Matisse's ''*The Joy of Life*'' and ''*Still Life with Flowers*'' showed that $CdCO_3$, CdC_2O_4, and $CdSO_4 \cdot nH_2O$ are degradation products. The distribution of various cadmium complexes confirms that cadmium carbonates and sulfates are products of photodegradation in ''*The Joy of Life*'', whereas in ''*Still Life with Flowers*'' cadmium carbonate appears to have been a starting reactant contained in the yellow paint. The authors of Ref. [354] analyzed yellow cadmium in Vincent Van Gogh's ''*Flowers in a Blue Vase*'' and showed that degradation triggers the disappearance of bright yellow color and the formation of white crystallites present in close to 50-μm globular aggregates on the paint surface. An analysis of a sample cross section made it possible to explain the complex degradation process.

10. Conclusion and outlook

It can be concluded from the foregoing that X-ray fluorescence imaging is one of the most efficient methods for the high-resolution nondestructive investigation of the distribution of various chemical elements with a submicrometer resolution in many inhomogeneous objects. However, it is not free from drawbacks. For example, the high intensity of an XR nanobeam may cause damage even to solid-state samples of condensed matter usually regarded as resistant to radiation. The likelihood of radiation damage can really restrict the spatial resolution of the method in many systems, such as polymers and biological objects, characterized by lower threshold radiation dose limits than metal and semiconductor systems. The goal is to gather a large set of data within short enough time intervals without detriment to their quality. This can be achieved through the following [6]:

(1) development of fast detectors with a large inlet window, low noise level, and large entrance solid angle;

(2) XR focusing with higher photon density to reduce exposure time without compromising the validity of statistical data in the measured signal;

(3) XR focusing onto a small spot to study small volumes owing to improved lateral resolution;

(4) experiments including fast processes (e.g., phase transitions) with rapid data recording to describe the kinetics of different processes and conduct *in situ* and *operando* studies;

(5) several simultaneous experimental studies with a single sample under identical conditions applying different methods;

(6) registering large complete datasets, e.g., imaging of large regions of reciprocal space. Fourth-generation SR sources [355] take advantage of significant improvements in accelerator technologies allowing us to draw closer to the diffraction limit for 'hard' photons. Such improvements of SR sources should be accompanied by the modernization of optics, detectors, and data analyzers to accumulate in full measure the benefits of new starting parameters of sources. It is hoped that focusing nanooptics approaching a 10-nm or higher spatial resolution will be available for routine experiments with nanometer-sized focal spots, opening up new prospects for 3D tomography and making possible even 4D measurements.

To reach the diffraction limit resolution in X-ray studies, coherent illumination is needed to derive benefits directly from the diffraction-limited storage rings under exploitation. Therefore, rapid measurements may prove beneficial, with the advent of such rings expected to produce a few orders of magnitude greater X-ray quanta fluxes [356].

The ability of an experimental station to dynamically change spatial resolution will probably become required, too. Finally, a combination of X-ray fluorescence imaging with other techniques will enhance the potential for studying a wide range of objects, but will also require the development of new algorithms for the comprehensive treatment of experimental data and artifact-free image reconstruction in a direct space.

List of abbreviations:

CCD — charge-coupled device
CDI — coherent diffraction imaging
CXFS — confocal X-ray fluorescence spectroscopy
E — X-ray energy
EXAFS — extended X-ray absorption fine structure
FF-XFM — full-field X-ray fluorescence microscopy
FTIR — Fourier transform infrared scanning
FZP — Fresnel zone plate
MDL — minimum detection limit
SDD — silicon drift detector
SR — synchrotron radiation
STXM — scanning transmission X-ray microscopy
SXFM — scanning X-ray fluorescence microscopy
SXFT — scanning X-ray fluorescence tomography
TER — total external reflection
XAFS — X-ray absorption fine structure spectroscopy
XANES — X-ray absorption near-edge structure spectroscopy
XBIC — X-ray beam-induced current
XFI — X-ray fluorescence imaging
XFT — X-ray fluorescence tomography
XR — X-ray
XRD — X-ray diffraction
XRF — X-ray fluorescence

References

1. Paunesku T et al. *J. Cell. Biochem.* **99** 1489 (2006)
2. Fahrni C J *Current Opin. Chem. Biol.* **11** 121 (2007)
3. Szczerbowska-Boruchowska M *X-Ray Spectrom.* **37** 21 (2008)
4. Pereira G R, Lopes R T, in *Biological Applications: Computed Tomography – Special Applications* (Ed. L Saba) (Rijeka: InTech, 2011) p. 153
5. Pushie M J et al. *Chem. Rev.* **114** 8499 (2014)
6. Somogyi A, Mocuta C *AIMS Mater. Sci.* **2** 122 (2015)
7. Revenko A G *Visn. Khar'kivskogo Nats. Univ. Khim.* **820** 39 (2008)
8. Bergmann U, Manning P L, Wogelius R A *Annu. Rev. Anal. Chem.* **5** 361 (2012)
9. Bertrand L et al. *Appl. Phys. A* **106** 377 (2012)
10. Punshon T, Guerinot M L, Lanzirotti A *Ann. Botany* **103** 665 (2009)
11. Lombi E, Susini J *Plant Soil* **320** 1 (2009)
12. Fittschen U E A, Falkenberg *Anal. Bioanal. Chem.* **400** 1743 (2011)
13. Donner E et al. *Anal. Bioanal. Chem.* **402** 3287 (2012)
14. Castillo-Michel H A et al. *Plant Physiol. Biochem.* **110** 13 (2017)
15. Alfeld M, de Viguerie L *Spectrochim. Acta B* **136** 81 (2017)
16. Janssens K et al. *Annu. Rev. Anal. Chem.* **6** 399 (2013)
17. Koval'chuk M V et al. *Crystallogr. Rep.* **61** 703 (2016); *Kristallografiya* **61** 681 (2016)
18. Bleuet P et al. *Trends Anal. Chem.* **29** 518 (2010)
19. de Jonge M D, Vogt S *Current Opin. Struct. Biol.* **20** 606 (2010)
20. Nikolaev V I, Chizhov E V *Nauchnoe Priborostroenie* **21** (2) 3 (2011)
21. Snigireva I, Snigirev A *J. Environ. Monit.* **8** 33 (2006)
22. Storizhko V E et al. *Usp. Fiz. Met.* **11** (1) 1 (2010)
23. Losev N F, Smagunova A N *Osnovy Rentgeno-Spektral'nogo Fluorestsentnogo Analiza* (Fundamentals of X-ray Fluorescence Analysis) (Moscow: Khimiya, 1982)
24. Anné J et al. *J. R. Soc. Interface* **11** 20140277 (2014)
25. Tsuji K, Nakano K *X-Ray Spectrom.* **36** 145 (2007)
26. Currie L A *Anal. Chem.* **40** 586 (1968)
27. Ortega R et al. *PloS ONE* **2** e925 (2007)
28. Chen S et al. *J. Synchrotron Rad.* **21** 66 (2014)
29. Harris H H et al. *J. Biol. Inorg. Chem.* **13** 303 (2008)
30. Dik J et al. *Anal. Chem.* **80** 6436 (2008)
31. Ravaud E et al. *Appl. Phys. A* **122** 17 (2016)
32. Edwards N P et al. *Appl. Phys. A* **111** 147 (2013)
33. Blokhin M A *Fizika Rentgenovskikh Luchei* (X-Ray Physics) (Moscow: GITTL, 1957)
34. Kirkpatrick P, Baez A V *J. Opt. Soc. Am.* **38** 766 (1948)
35. Howells M R et al. *Opt. Eng.* **39** 2748 (2000)
36. Ortega R et al. *Anal. Chem.* **76** 309 (2004)
37. Philip R et al. *Appl. Opt.* **27** 1918 (1988)
38. Erko A et al. *J. Synchrotron Rad.* **5** 239 (1998)
39. Bourgeois D et al. *Anal. Bioanal. Chem.* **407** 6619 (2015)
40. Rak M et al. *Anal. Bioanal. Chem.* **406** 2809 (2014)
41. Laforce B et al. *Sci. Rep.* **6** 29999 (2016)
42. Matsuyama S et al. *X-Ray Spectrom.* **38** 89 (2009)
43. Barrett R et al. *Proc. SPIE* **8139** 813904 (2011)
44. Gil S et al. *Biol. Trace Elem. Res.* **163** 177 (2015)
45. Attwood D T *Soft X-Rays and Extreme Ultraviolet Radiation: Principles and Applications* (Cambridge: Cambridge Univ. Press, 2000)
46. Wu S-R, Hwu Y, Margaritondo G *Materials* **5** 1752 (2012)
47. Michette A G *Optical Systems for Soft X-Rays* (New York: Plenum Press, 1986); Translated into Russian: *Optika Myagkogo Rentgenovskogo Izlucheniya* (Moscow: Mir, 1989)
48. Lider V V *J. Surf. Invest. X-Rays, Synch. Neutron Tech.* **11** 1113 (2017); *Poverkhnost'* (11) 7 (2017)
49. Kirz J *J. Opt. Soc. Am.* **64** 301 (1974)
50. Yun W et al. *Rev. Sci. Instrum.* **70** 2238 (1999)
51. Watanabe N et al. *J. Phys. Conf. Ser.* **186** 012022 (2009)
52. Bertoni M I et al. *Energy Environ. Sci.* **4** 4252 (2011)
53. Finney L et al. *Proc. Natl. Acad. Sci. USA* **104** 2247 (2007)
54. Gu B et al. *Biogeosciences* **11** 5259 (2014)
55. Mustafi D et al. *Mol. Imaging* **14** 7290 (2015)
56. Dillon C T et al. *J. Biol. Inorg. Chem.* **7** 640 (2002)
57. de Jonge M D et al. *Proc. Natl. Acad. Sci. USA* **107** 15676 (2010)
58. Arkad'ev V A et al. *Sov. Phys. Usp.* **32** 271 (1989); *Usp. Fiz. Nauk* **157** 529 (1989)
59. Dabagov S B *Phys. Usp.* **46** 1053 (2003); *Usp. Fiz. Nauk* **173** 1083 (2003)
60. Bilderback D H *X-Ray Spectrom.* **32** 195 (2003)
61. Charnley N R, Potts P J, Long J V P *J. Anal. At. Spectrom.* **9** 1185 (1994)
62. Bjeoumikhov A, Bjeoumikhova S, Wedell R *Part. Part. Syst. Charact.* **22** 384 (2005)
63. De Nolf W, Janssens K *Surf. Interface Anal.* **42** 411 (2010)
64. Thiel D J et al. *Nucl. Instrum. Meth. Phys. Res. A* **317** 597 (1992)

65. Bilderback D H, Hoffman S A, Thiel D J *Science* **263** 201 (1994)
66. Hoffman S A, Thiel D J, Bilderback D H *Nucl. Instrum. Meth. Phys. Res. A* **347** 384 (1994)
67. Vincze L et al. *Adv. X-Ray Anal.* **41** 252 (1999)
68. Kumakhov M A *Nucl. Instrum. Meth. Phys. Res. B* **48** 283 (1990)
69. Kumakhov M A, Komarov F F *Phys. Rep.* **191** 289 (1990)
70. Kumakhov M A *X-Ray Spectrom.* **29** 343 (2000)
71. Gao N, Janssens K, in *X-Ray Spectrometry*: *Recent Technological Advances* (Eds K Tsuji, J Injuk, R Van Grieken) (Chichester: Wiley, 2004) p. 89
72. Bolotkov A et al. *Analitika* (4) 14 (2012)
73. MacDonald C A *X-Ray Opt. Instrum.* **2010** 867049 (2010)
74. Wegrzynek D et al. *X-Ray Spectrom.* **37** 635 (2008)
75. Sun T et al. *Spectrochim. Acta B* **64** 1194 (2009)
76. Aristov V V, Shabel'nukov L G *Phys. Usp.* **51** 57 (2008); *Usp. Fiz. Nauk* **178** 61 (2008)
77. Snigirev A et al. *Nature* **384** 49 (1996)
78. Snigirev A et al. *Appl. Opt.* **37** 653 (1998)
79. Lengeler B et al. *J. Appl. Phys.* **84** 5855 (1998)
80. Lengeler B et al. *J. Synchrotron Rad.* **6** 1153 (1999)
81. Schroer C G et al. *Proc. SPIE* **4145** 274 (2001)
82. Piestrup M A et al. *Rev. Sci. Instrum.* **71** 4375 (2000)
83. Dudchik Yu I et al. *Spectrochim. Acta B* **62** 598 (2007)
84. Lengeler B et al. *Appl. Phys. Lett.* **74** 3924 (1999)
85. Lengeler B et al. *J. Phys. D* **38** 218 (2005)
86. Kulipanov G N *Phys. Usp.* **50** 368 (2007); *Usp. Fiz. Nauk* **111** 384 (2007)
87. Kunz C *J. Phys. Condens. Matter* **13** 7499 (2001)
88. Evans-Lutterodt K et al. *Opt. Exp.* **11** 919 (2003)
89. Stein A et al. *J. Vac. Sci. Technol. B* **26** 122 (2008)
90. Snigirev A et al. *J. Phys. Conf. Series* **186** 012072 (2009)
91. Szlachetko J et al. *J. Synchrotron Rad.* **17** 400 (2010)
92. Chen H, Rogalski M M, Anker J N *Phys. Chem. Chem. Phys.* **14** 13469 (2012)
93. Cesareo R, Ettore Gigante G, Castellano A *Nucl. Instrum. Meth. Phys. Res. A* **428** 171 (1999)
94. Strüder L *Nucl. Instrum. Meth. Phys. Res. A* **454** 73 (2000)
95. Schlosser D M et al. *Nucl. Instrum. Meth. Phys. Res. A* **624** 270 (2010)
96. Gianoincelli A et al. *Appl. Phys. Lett.* **89** 251117 (2006)
97. Alfeld M et al. *Appl. Phys. A* **111** 165 (2013)
98. Longoni A et al. *X-ray Spectrometry* **34** 439 (2005)
99. Alberti R et al. *Nucl. Instrum. Meth. Phys. Res. A* **580** 1004 (2007)
100. Ryan C G et al. *J. Phys. Conf. Ser.* **499** 012002 (2014)
101. Tomik B et al. *Neurochem. Res.* **31** 321 (2006)
102. Cotte M et al. *Acc. Chem. Res.* **43** 705 (2010)
103. Haschke M et al. *Adv. X-Ray Anal.* **55** 286 (2012)
104. Lombi E et al. *Anal. Bioanal. Chem.* **400** 1637 (2011)
105. Donner E et al., in *Plant Mineral Nutrients*: *Methods and Protocols* (Ed. F J M Maathuis) (New York: Springer, 2013) p. 143
106. Garrevoet J et al. *Anal. Chem.* **87** 6544 (2015)
107. Laforce B et al. *Anal. Chem.* **88** 3386 (2016)
108. Vekemans B et al. *X-Ray Spectrom.* **26** 333 (1997)
109. Alfeld M, Janssens K *J. Anal. At. Spectrom.* **30** 777 (2015)
110. Vekemans B et al. *X-Ray Spectrom.* **23** 278 (1994)
111. Solé V A et al. *Spectrochim. Acta B* **62** 63 (2007)
112. Vogt S *J. Phys. IV France* **104** 635 (2003)
113. Ryan C G et al. *Nucl. Instrum. Meth. Phys. Res. B* **231** 183 (2005)
114. Ryan C G et al. *Nucl. Instrum. Meth. Phys. Res. B* **47** 55 (1990)
115. Janssens K et al. *TrAC Trends Anal. Chem.* **29** 464 (2010)
116. Sherman J *Spectrochimica Acta* **7** 283 (1955–1956)
117. Shiraiwa T, Fujino N *Jpn. J. Appl. Phys.* **5** 886 (1966)
118. Elam W T et al. *Adv. X-Ray Anal.* **47** 104 (2004)
119. Lopes R T et al. *Pramana J. Phys.* **76** 271 (2011)
120. Bohic S et al. *Appl. Phys. Lett.* **78** 3544 (2001)
121. Twining B S et al. *Anal. Chem.* **75** 3806 (2003)
122. Kemner K M et al. *Science* **306** 686 (2004)
123. Jensen M P et al. *Nature Chem. Biol.* **7** 560 (2011)
124. Cardoso S C et al. *PLoS ONE* **6** e29244 (2011)
125. Ortega R et al. *J. R. Soc. Interface* **6** S649 (2009)
126. Qin Z et al. *Metallomics* **3** 28 (2011)
127. Farquharson M J et al. *Appl. Radiat. Isotopes* **65** 183 (2007)
128. Carmona A et al. *J. Anal. At. Spectrom.* **23** 1083 (2008)
129. Kehr S et al. *J. Mol. Biol.* **389** 808 (2009)
130. Duong T T H et al. *J. Neurochem.* **108** 1143 (2009)
131. Kim A M et al. *Nature Chem. Biol.* **6** 674 (2010)
132. Zhang J Z et al. *Integr. Biol.* **4** 1072 (2012)
133. Ceko M J et al. *Biol. Reprod.* **94** 86 (2016)
134. Bohic S et al. *Anal. Chem.* **80** 9557 (2008)
135. Popescu B F G et al. *Phys. Med. Biol.* **54** 651 (2009)
136. Chwiej J et al. *J. Biol. Inorg. Chem.* **15** 283 (2010)
137. Kaščáková S et al. *J. Path. Clin. Res.* **2** 175 (2016)
138. Ide-Ektessabi A et al. *X-Ray Spectrom.* **31** 7 (2002)
139. Shimura M et al. *Cancer Res.* **65** 4998 (2005)
140. Chen K G et al. *Proc. Natl. Acad. Sci. USA* **103** 9903 (2006)
141. Yuan Y et al. *ACS Nano* **7** 10502 (2013)
142. Sheridan E J et al. *J. Synchrotron Rad.* **20** 226 (2013)
143. Palmer B M et al. *J. Struct. Biol.* **155** 12 (2006)
144. Qin Z, Toursarkissian B, Lai B *Metallomics* **3** 823 (2011)
145. House M J et al. *J. Cardiovasc. Magn. Reson.* **16** 80 (2014)
146. Korbas M et al. *Proc. Natl. Acad. Sci. USA* **105** 12108 (2008)
147. Korbas M et al. *ACS Chem. Biol.* **8** 2256 (2013)
148. Harris H H et al. *J. Synchrotron Rad.* **15** 123 (2008)
149. Sarret G et al. *Adv. Agron.* **119** 1 (2013)
150. Jiménez S et al. *Plant Soil* **315** 93 (2009)
151. Takahashi M et al. *Plant Soil* **325** 39 (2009)
152. Lombi E et al. *New Phytologist* **184** 193 (2009)
153. Lombi E et al. *J. Exp. Bot.* **62** 273 (2011)
154. Neidhardt H et al. *Chem. Erde Geochem.* **75** 261 (2015)
155. Hosokawa Y et al. *X-Ray Spectrom.* **26** 380 (1997)
156. Lanzirotti A et al. *J. Archaeol. Sci.* **52** 204 (2014)
157. Noguchi T et al., in *Interdisciplinary Studies on Environmental Chemistry-Environmental Pollution and Ecotoxicology* (Eds M Kawaguchi et al.) (Tokyo: TERRAPUB, 2012) p. 73
158. Holt M et al. *Annu. Rev. Mater. Res.* **43** 183 (2013)
159. Gianoncelli A et al. *X-Ray Spectrom.* **44** 263 (2015)
160. Istratov A A et al. *J. Appl. Phys.* **94** 6552 (2003)
161. Buonassisi T et al. *J. Appl. Phys.* **97** 074901 (2005)
162. Kwapil W et al. *Appl. Phys. Lett.* **95** 232113 (2009)
163. Macdonald D et al. *Phys. Status Solidi A* **207** 1807 (2010)
164. Kramar U et al. *Spectrochim. Acta B* **62** 824 (2007)
165. Laforce B et al. *Anal. Chem.* **86** 12369 (2015)
166. Frisia S et al. *Archaeometry* **47** 209 (2005)
167. Frisia S et al. *Clim. Past* **8** 2039 (2012)
168. Ishii H A et al. *Meteorit. Planet. Sci.* **43** 215 (2008)
169. Provis J L et al. *Cement Concr. Compos.* **36** 56 (2013)
170. Dumont M et al. *Powder Diffraction* **24** 130 (2009)
171. Limburg K E, Huang R, Bilderback D H *X-Ray Spectrom.* **36** 336 (2007)
172. Cook P K et al. *Chem. Geol.* **14** 1 (2015)
173. Alfeld M et al. *Appl. Phys. A* **111** 157 (2013)
174. Dredge P et al. *Appl. Phys. A* **121** 789 (2015)
175. Thurrowgood D et al. *Sci. Rep.* **6** 29594 (2016)
176. Popelka-Filcoff R S et al. *Analyst* **141** 3657 (2016)
177. Alfeld M et al. *J. Anal. At. Spectrom.* **8** 760 (2013)
178. Bronk H et al. *Fresenius' J. Anal. Chem.* **371** 307 (2001)
179. Trentelman K et al. *X-Ray Spectrom.* **39** 159 (2010)
180. Trentelman K et al. *Appl. Phys. A* **121** 801 (2015)
181. Martins A et al. *Heritage Sci.* **4** 22 (2016)
182. Martins A et al. *Heritage Sci.* **4** 33 (2016)
183. Duivenvoorden J R et al. *Heritage Sci.* **5** 6 (2017)
184. Scott D A *Archaeometry* **43** 475 (2001)
185. Mantler M, Schreiner M *X-Ray Spectrom.* **29** 3 (2000)
186. Hocquet F-P et al. *Anal. Bioanal. Chem.* **399** 3109 (2011)
187. Alfeld M et al. *J. Anal. At. Spectrom.* **26** 899 (2011)
188. Seim C et al. *J. Anal. At. Spectrom.* **29** 1354 (2014)
189. Strivay D et al. *Appl. Phys. A* **122** 950 (2016)
190. Bull D et al. *Burlingt. Mag.* **153** 668 (2011)
191. Alfeld M et al. *J. Anal. At. Spectrom.* **28** 40 (2013)
192. Van der Snickt G et al. *Appl. Spectrosc.* **70** 57 (2016)
193. van Eikema Hommes M et al. *Rijksmuseum Bull.* **64** 4 (2016)
194. Anitha A et al. *Signal Process.* **93** 592 (2013)
195. Eveno M et al. *Heritage Sci.* **2** 17 (2014)
196. Janssens K et al. *Microchem. J.* **126** 515 (2016)
197. Ricciardi P et al. *Microchem. J.* **124** 785 (2016)
198. Bergmann U *Phys. World* **20** (11) 39 (2007)

199. Gibson W M, Kumakhov M A *Proc. SPIE* **1736** 172 (1993)
200. Ding X, Gao N, Havrilla G J *Proc. SPIE* **4144** 174 (2000)
201. Nakano K, Tsuji K *J. Anal. At. Spectrom.* **25** 562 (2010)
202. Sun T, Ding X *Rev. Anal. Chem.* **34** 45 (2015)
203. Woll A R et al. *J. Phys. Conf. Ser.* **493** 012028 (2014)
204. Nakazawa T, Tsuji K *X-Ray Spectrom.* **42** 374 (2013)
205. Kanngießer B et al. *Spectrochim. Acta B* **60** 41 (2005)
206. Xiaoyan L et al. *Nucl. Instrum. Meth. Phys. Res. B* **266** 2638 (2008)
207. Mantouvalou I et al. *J. Anal. At. Spectrom.* **25** 554 (2010)
208. Laclavetine K et al. *Microchem. J.* **125** 62 (2016)
209. Kanngießer B et al. *Appl. Phys. A* **106** 325 (2012)
210. Tsuji K, Nakano K *J. Anal. At. Spectrom.* **26** 305 (2011)
211. Senkbeil T et al. *Anal. Bioanal. Chem.* **408** 1487 (2016)
212. Zoeger N et al. *X-Ray Spectrom.* **37** 3 (2008)
213. Šmit Ž et al. *Nucl. Instrum. Meth. Phys. Res. B* **219 – 220** 35 (2004)
214. Vekemans B et al. *J. Anal. At. Spectrom.* **19** 1302 (2004)
215. Malzer W, Kanngießer B *Spectrochim. Acta B* **60** 1334 (2005)
216. Schmitz S et al. *Geochim. Cosmochim. Acta* **73** 5483 (2009)
217. Mantouvalou I et al. *Anal. Chem.* **80** 819 (2008)
218. Sokaras D, Karydas A-G *Anal. Chem.* **81** 4946 (2009)
219. de Viguerie L, Solé V A, Walter P *Anal. Bioanal. Chem.* **395** 2015 (2009)
220. Czyzycki M et al. *X-Ray Spectrom.* **40** 88 (2011)
221. Perez R D et al. *X-Ray Spectrom.* **40** 19 (2011)
222. Schoonjans T et al. *Spectrochim. Acta B* **67** 32 (2012)
223. Mantouvalou I, Malzer W, Kanngießer B *Spectrochim. Acta B* **77** 9 (2012)
224. Mantouvalou I et al. *Anal. Chem.* **86** 9774 (2014)
225. Szalóki I et al. *J. Anal. At. Spectrom.* **32** 334 (2017)
226. Kanngießer B, Malzer W, Reiche I *Nucl. Instrum. Meth. Phys. Res. B* **211** 259 (2003)
227. Woll A R et al. *Mater. Res. Soc. Symp. Proc.* **852** 281 (2005)
228. Woll A R et al. *Studies Conservation* **53** 93 (2008)
229. Malzer W *Rigaku J.* **23** 40 (2006)
230. Reiche I et al. *J. Anal. At. Spectrom.* **27** 1715 (2012)
231. Reiche I et al. *Appl. Phys. A* **121** 903 (2015)
232. Kanngießer B et al. *J. Anal. At. Spectrom.* **23** 814 (2008)
233. Nakano K, Tsuji K *X-Ray Spectrom.* **38** 446 (2009)
234. Nakazawa T, Tsuji K *X-Ray Spectrom.* **42** 123 (2013)
235. Nakano K et al. *ISIJ Int.* **53** 1953 (2013)
236. Akioka K et al. *Powder Diffraction* **29** 151 (2014)
237. Tsuji K, Yonehara T, Nakano K *Anal. Sci.* **24** 99 (2008)
238. Perez R D et al. *Radiat. Phys. Chem.* **79** 195 (2010)
239. McCormick N et al. *PLoS ONE* **5** e11078 (2010)
240. Vincze L et al. *Anal. Chem.* **76** 6786 (2004)
241. Schmitz S et al. *Eur. J. Mineral.* **21** 927 (2009)
242. Choudhury S et al. *Archaeometry* **58** (S1) 207 (2016)
243. Choudhury S et al. *J. Anal. At. Spectrom.* **32** 527 (2017)
244. Nakano K et al. *Anal. Chem.* **83** 3477 (2011)
245. Emoto S et al. *Adv. X-Ray Anal.* **56** 217 (2013)
246. Mazel V et al. *Talanta* **85** 556 (2011)
247. Mihucz V G et al. *Food Chem.* **121** 290 (2010)
248. Vasin M G et al. *Spectrochim. Acta B* **62** 648 (2007)
249. Bruyndonckx P, Sasov A, Liu X *AIP Conf. Proc.* **1365** 61 (2011)
250. Ordavo I et al. *Nucl. Instrum. Meth. Phys. Res. A* **654** 250 (2011)
251. Romano F P et al. *Anal. Chem.* **86** 10892 (2014)
252. Dudchik Yu I, Khil'ko G I, Lomashko O K *Pribory Metody Izmerenii* **1** (2) 169 (2016)
253. Silva A L M et al. *Spectrochimica Acta B* **66** 308 (2011)
254. Uher J, Harvey G, Jakubek J *IEEE Trans. Nucl. Sci.* **59** 1067 (2010)
255. Žemlička J et al. *Nucl. Instrum. Meth. Phys. Res. A* **607** 202 (2009)
256. Bjeoumikhov A et al. *JINST* **7** C11008 (2012)
257. Silva A L M et al. *J. Anal. At. Spectrom.* **30** 343 (2015)
258. Davis J M et al. *Microsc. Microanal.* **21** (S3) 1637 (2015)
259. Mutina A, Bruyndonckx P *Microscopy Analysis* **27** (4) (2013); https://microscopy-analysis.com/sites/default/files/2013_May_Mutina.pdf
260. Aoki S, Takeuchi A, Ando M *J. Synchrotron Rad.* **5** 1117 (1998)
261. Watanabe N et al. *Nucl. Instrum. Meth. Phys. Res. A* **467 – 468** 837 (2001)
262. Ohigashi T et al. *J. Synchrotron Rad.* **9** 128 (2002)
263. Hoshino M et al. *Rev. Sci. Instrum.* **78** 073706 (2007)
264. Underwod J H, Attwood D T *Phys. Today* **37** (4) 44 (1984); *Usp. Fiz. Nauk* **151** 105 (1987)
265. Hoshino M et al. *Proc. SPIE* **5533** 85 (2004)
266. Reiche I et al. *Anal. Chem.* **85** 5857 (2013)
267. Zielińska A et al. *JINST* **8** P10011 (2013)
268. Fu G et al. *Med. Phys.* **40** 061903 (2013)
269. Garrevoet J et al. *Anal. Chem.* **86** 11826 (2014)
270. Kinney J H et al. *Nucl. Instrum. Meth. Phys. Res. A* **347** 480 (1994)
271. Boisseau P, Grodzins L *Hyperfine Interact.* **33** 283 (1987)
272. Yuasa T, Takeda T, in *Molecular Imaging* (Ed. B Schaller) (Zagreb: InTechOpen, 2012) p. 39
273. Simionovici A et al. *IEEE Trans. Nucl. Sci.* **47** 2736 (2000)
274. Schroer C G et al. *Proc. SPIE* **4503** 230 (2002)
275. Brunetti A, Golosio B *Comput. Phys. Commun.* **141** 412 (2001)
276. Miqueles E X, De Pierro A R *Phys. Med. Biol.* **55** 1007 (2010)
277. Gürsoy D et al. *Opt. Express* **23** 9014 (2015)
278. Di Z, Leyffer S, Wild S *SIAM J. Imaging Sci.* **9** 1 (2016)
279. Kak A C, Slaney M *Principles of Computerized Tomographic Imaging* (New York: IEEE Press, 1988)
280. Qi J, Leahy R M *Phys. Med. Biol.* **51** R541 (2006)
281. Golosio B et al. *J. Appl. Phys.* **94** 145 (2003)
282. Rust G- F, Weigelt J *IEEE Trans. Nucl. Sci.* **45** 75 (1998)
283. La Rivière P J et al. *Opt. Eng.* **45** 077005 (2006)
284. Yang Q et al. *J. Synchrotron Rad.* **19** 210 (2012)
285. Miqueles E, De Pierro A R *J. Phys. Conf. Ser.* **410** 012167 (2013)
286. Hogan J P, Gonsalves R A, Krieger A S *IEEE Trans. Nucl. Sci.* **38** 1721 (1991)
287. Yuasa T et al. *IEEE Trans. Nucl. Sci.* **44** 54 (1997)
288. Schroer C G *Appl. Phys. Lett.* **79** 1912 (2001)
289. Bruyndonckx P et al. *Proc. SPIE* **7804** 78041A (2010)
290. De Samber B et al. *Anal. At. Spectrom.* **25** 544 (2010)
291. Pereira G. R et al. *J. Radioanal. Nucl. Chem.* **269** 469 (2006)
292. Pereira G R et al. *X-Ray Spectrom.* **38** 244 (2009)
293. Takeda T et al. *J. Synchrotron Radiat.* **16** 57 (2009)
294. Thet-Thet-Lwin, Takeda T, Wu J *J. Synchrotron Rad.* **15** 528 (2008)
295. Lombi E et al. *PLoS ONE* **6** e20626 (2011)
296. Camerani M C et al. *Anal. Chem.* **76** 1586 (2004)
297. De Samber B et al. *J. Anal. At. Spectrom.* **23** 829 (2008)
298. Mishra S et al. *J. Exp. Bot.* **67** 4639 (2016)
299. Naghedolfeizi M et al. *J. Nucl. Mater.* **312** 146 (2003)
300. McNear D H et al. *Environ. Sci. Technol.* **39** 2210 (2005)
301. Tappero R et al. *New Phytologist* **175** 641 (2007)
302. Zhang M et al. *HortScience* **50** 801 (2015)
303. Kim S A et al. *Science* **314** 1295 (2006)
304. Cotte M et al. *J. Anal. At. Spectrom.* **23** 820 (2008)
305. Rehr J J, Albers R C *Rev. Mod. Phys.* **72** 621 (2000)
306. Scheckel K G et al. *Environ. Sci. Technol.* **38** 5095 (2004)
307. Kopittke P M et al. *Plant Physiol.* **156** 663 (2011)
308. Huguet S et al. *E3S Web Conf.* **1** 19008 (2013)
309. Isaure M-P et al. *J. Exp. Botany* **66** 3201 (2015)
310. Yoshida S, Ide-Ektessabi A, Fujisawa S *Struct. Chem.* **14** 85 (2003)
311. Harris H H et al. *J. Biol. Inorg. Chem.* **10** 105 (2005)
312. Farquharson M J et al. *Med. Biol.* **53** 3023 (2008)
313. Hummer A A, Rompel A *Metallomics* **5** 597 (2013)
314. Collingwood J F, Davidson M R *Front. Pharmacol.* **5** 191 (2014)
315. Sugiyama T et al. *Biometals* **28** 11 (2015)
316. Smith E et al. *Chemosphere* **76** 529 (2009)
317. Monico L et al. *J. Anal. At. Spectrom.* **30** 613 (2015)
318. Gay M et al. *J. Anal. At. Spectrom.* **30** 767 (2015)
319. Grolimund D et al. *Spectrochim. Acta B* **59** 1627 (2004)
320. Cotte M et al. *Anal. Chem.* **78** 7484 (2006)
321. Van der Snickt G et al. *Anal. Chem.* **81** 2600 (2009)
322. Blute N K et al. *Environ. Sci. Technol.* **38** 6074 (2004)
323. Ide-Ektessabi A, Rabionet M *Anal. Sci.* **21** 885 (2005)
324. Ortega R et al. *Chem. Res. Toxicol.* **18** 1512 (2005)
325. Pickering I J et al. *Environ. Sci. Technol.* **40** 5010 (2006)
326. Bulska E et al. *Anal. Chem.* **78** 7616 (2006)
327. Cotte M et al. *Anal. Chem.* **79** 6988 (2007)
328. Etschmann B E et al. *Am. Mineral.* **95** 884 (2010)
329. Monico L et al. *Anal. Chem.* **83** 1224 (2011)
330. Hall C *JINST* **8** C06007 (2013)
331. Hong Y P et al. *J. Synchrotron Rad.* **21** 229 (2014)
332. Hong Y P, Chen S, Jacobsen C *Proc. SPIE* **9592** 95920W (2015)
333. Hornberger B et al. *J. Synchrotron Rad.* **15** 355 (2008)
334. Vine D J et al. *Opt. Express* **20** 18287 (2012)

335. Deng J et al. *Proc. Natl. Acad. Sci. USA* **112** 2314 (2015)
336. Chen S et al. *Microsc. Microanal.* **22** (S3) 90 (2016)
337. Lind O C et al. *J. Environ. Radioactiv.* **123** 63 (2013)
338. Bernal S A et al. *J. Am. Ceramic Soc.* **96** 1951 (2013)
339. Jaroszewicz J et al. *Anal. Bioanal. Chem.* **391** 1129 (2008)
340. Vyvenko O F et al. *J. Appl. Phys.* **91** 3614 (2002)
341. Villanova J et al. *J. Synchrotron Rad.* **19** 521 (2012)
342. Edwards N P et al. *Proc. R. Soc. Lond. B* **278** 3209 (2011)
343. Miller L M et al. *J. Struct. Biol.* **155** 30 (2006)
344. Segura-Ruiz J et al. *Nano Lett.* **14** 1300 (2014)
345. Manceau A et al. *Am. Mineral.* **87** 1494 (2002)
346. Lind O C et al. *J. Environ. Radioact.* **81** 21 (2005)
347. Denecke M A et al. *AIP Conf. Proc.* **882** 187 (2007)
348. Denecke M A et al. *J. Phys. Conf. Ser.* **190** 012187 (2009)
349. Terzano R et al. *Environ. Pollut.* **158** 2702 (2010)
350. Radepont M et al. *J. Anal. At. Spectrom.* **26** 959 (2011)
351. Szczerbowska-Boruchowska M et al. *X-Ray Spectrom.* **34** 514 (2005)
352. Trushin M et al. *Nucl. Instum. Meth. Phys. Res. B* **268** 254 (2010)
353. Pouyet E et al. *Appl. Phys. A* **121** 967 (2015)
354. Van der Snickt G, Janssens K, Dik J *Anal. Chem.* **84** 10221 (2012)
355. Bilderback D H, Elleaume P, Weckert E *J. Phys. B* **38** S773 (2005)
356. de Jonge M D, Ryan C G, Jacobsen C J *J. Synchrotron Rad.* **21** 1031 (2014)